Formation of droplets in microfluidic cross-junctions at small capillary numbers

Breakdown of the classical squeezing regime

Kurniawan, Tetuko; Sahebdivani, Mahsa; Zaremba, Damian; Blonski, Slawomir; Garstecki, Piotr; van Steijn, Volkert; Korczyk, Piotr M.

DOI
10.1016/j.cej.2023.145601

Publication date
2023

Document Version
Final published version

Published in
Chemical Engineering Journal

Citation (APA)
Kurniawan, T., Sahebdivani, M., Zaremba, D., Blonski, S., Garstecki, P., van Steijn, V., & Korczyk, P. M. (2023). Formation of droplets in microfluidic cross-junctions at small capillary numbers: Breakdown of the classical squeezing regime. *Chemical Engineering Journal*, *474*, Article 145601. https://doi.org/10.1016/j.cej.2023.145601

Chemical Engineering Journal 474 (2023) 145601

Contents lists available at ScienceDirect

Chemical Engineering Journal

journal homepage: www.elsevier.com/locate/cej

Formation of droplets in microfluidic cross-junctions at small capillary numbers: Breakdown of the classical squeezing regime

Tetuko Kurniawan [a,b,*], Mahsa Sahebdivani [c], Damian Zaremba [a], Slawomir Blonski [a], Piotr Garstecki [c], Volkert van Steijn [d,*], Piotr M. Korczyk [a,*]

[a] Institute of Fundamental Technological Research, Polish Academy of Sciences, Pawinskiego 5B, 02-106 Warsaw, Poland
[b] President University, Jl. Ki Hajar Dewantara, Kota Jababeka, Bekasi 17550, Indonesia
[c] Institute of Physical Chemistry, Polish Academy of Sciences, Kasprzaka 44/52, 01-224 Warsaw, Poland
[d] Delft University of Technology, Faculty of Applied Sciences, Dept. Chemical Engineering, van der Maasweg 9, 2629 HZ Delft, the Netherlands

ARTICLE INFO

Keywords:
Microfluidics
Cross-junction
Flow-focusing device
Droplet formation
Two-phase flow
Scaling law
Squeezing regime

ABSTRACT

Two decades of research on droplet formation in microchannels have led to the widely accepted view that droplets form through the squeezing mechanism when interfacial forces dominate over viscous forces. The initially surprising finding that the volume of the droplets is insensitive to the relative importance of these two forces is nowadays well understood from the constrained deformation of the droplet interface during formation. In this work, we show a lower limit of the squeezing mechanism for droplets produced in microfluidic cross-junctions. Below this limit, in the leaking regime, which was recently discovered for droplets produced in T-junctions, the volume of the produced droplets strongly depends on the relative importance of interfacial and viscous forces, as captured by the capillary number. We reveal a fundamental difference in the mechanisms at play in the leaking regime between T- and cross-junctions. In cross-junctions, the droplet neck elongates substantially, and unlike the case of the T-junction, the magnitude of this elongation depends strongly on the value of the capillary number. This elongation significantly affects the final droplet volume in a low capillary number regime. Generalizing the classical squeezing law by lifting the original assumptions and incorporating both identified mechanisms of leaking through gutters and neck elongation, we derive a model for droplet formation and show that it agrees with our experiments.

1. Introduction

Droplet microfluidics [1–3] is a field of research driven by the development of applications that utilize droplets as microreactors for biochemical analysis [4,5], continuous flow synthesis [6], and biomedical (point-of-care) diagnostics [7–11]. Additionally, droplets can be used as building blocks for the development of advanced materials, including catalytic nanoparticles, designer emulsions, and tissue, with applications in the pharmaceutical [12–16], cosmetic [17], and food industries [18]. All this work relies on the ability to generate droplets controllably. This requires a thorough mechanistic understanding of droplet formation to know how to tune the volume of the droplets for given fluid properties, flow conditions, and channel geometries.

One of the geometries generally used for droplet generation is the junction shown in Fig. 1a, where the liquid phase from which droplets are produced is engulfed by another liquid phase in which the produced droplets are immiscible and carried along. This so-called “cross-junction”, considered in this work, can be seen as the most straightforward flow-focusing geometry, i.e., one without constriction in the main channel. The typical size of the main channel is between a few tens and up to a few hundreds of micrometers. At such length scales, the flow is governed by viscous or interfacial forces for a large operation window, with a minor role for body forces such as gravity and inertia.

Different multiphase flow regimes can be obtained by tuning the relative importance of viscous and interfacial forces [19,20], as commonly captured by the capillary number Ca. Two decades of work

* Corresponding authors at: Institute of Fundamental Technological Research, Polish Academy of Sciences, Pawinskiego 5B, 02-106 Warsaw, Poland (T. Kurniawan, P. M. Korczyk). Delft University of Technology, Faculty of Applied Sciences, Dept. Chemical Engineering, van der Maasweg 9, 2629 HZ Delft, the Netherlands (V. van Steijn)

E-mail addresses: tetuko@president.ac.id, tkurniaw@ippt.pan.pl (T. Kurniawan), v.vanSteijn@tudelft.nl (V. van Steijn), piotr.korczyk@ippt.pan.pl (P.M. Korczyk).

https://doi.org/10.1016/j.cej.2023.145601
Received 24 May 2023; Received in revised form 5 August 2023; Accepted 21 August 2023
Available online 22 August 2023

Nomenclature

A Time-dependent factor scaling the shape of the neck in the direction perpendicular to the main channel axis [m]
$a = A/W$ Dimensionless A
a_0 Dimensionless A, at the initial time of the neck relaxation
A_G The cross-sectional area of the gutter [m^2]
$b = \kappa/Ca$ Dimensionless fitting parameter
$Ca = \frac{U_C \mu_C}{\gamma} = \frac{Q_C \mu_C}{WH\gamma}$ Capillary number
E Local maxima or minima of the width of the forming droplet [m]
H The height of the microchannel [m]
$h(x)$ Approximation of the two-dimensional shape of the neck as it appears in a top-view image [m]
K_F The curvature at the front of the forming droplet [1/m]
K_N The curvature of the interface at the neck region [1/m]
L_0 The initial length of the droplet or gutter [m]
$l_0 = V_0/HW^2$ The dimensionless volume of the forming droplet at the start of the necking stage, $\tau = 0$ s
$l_D = V_D/HW^2$ The dimensionless volume of the droplet
L_T The distance measured from the tip of the forming droplet to the edge of the cross-junction inlet [m]
L_{T0} The distance measured from the tip of the forming droplet to the edge of the cross-junction inlet at the beginning of the necking stage [m]
p Constant parameter represents τ^* at the high Ca regime
$q = Q_D/Q_C$ Flow rate ratio between DP and CP
Q_B Rate of flow of the CP bypassing a droplet through the gutters in the corners of the channel [m^3/s]
Q_C Rate of flow of the CP [m^3/s]
Q_D Rate of flow of the DP [m^3/s]
$Q_G = Q_B/4$ Rate of flow of the CP bypassing a droplet through the single gutter, [m^3/s]
Q_N Rate of flow of the CP filling the volume V_N [m^3/s]
$\langle Q_N \rangle$ Time-average of Q_N [m^3/s]
$q_N = Q_N/Q_C$ Fraction of CP flow that forms the neck
$\langle q_N \rangle$ Time-average of q_N
t Time [s]
$t^* = tQ_C/W^2H$ Dimensionless time
$U_C = Q_C/WH$ The mean velocity of the CP [m/s]
V_0 The volume of a forming droplet at the end of the filling stage [m^3]
$v_0 = a_0\omega_0$ Dimensionless volume at the initial time of neck relaxation
V_D The final volume of a droplet [m^3]
V_N The volume of the CP collected behind the forming droplet [m^3]
$v_N = V_N/HW^2$ The dimensionless instantaneous volume of the CP collected behind the forming droplet
$V_{N0} = V_N(\tau)$ The volume of the CP collected behind the forming droplet at the end of the necking stage [m^3]
$v_{NO} = V_{N0}/HW^2$ The dimensionless volume of the CP collected behind the forming droplet at the end of the necking stage
W Width of the channel [m]

Greek Symbols

α The correction factor of the specific cross-section of the gutter
β A constant parameter in the T-junction device that approximates the boundary between the squeezing and leaking regime
γ Interfacial tension [N/m]
$\Delta p_L = \gamma(K_F - K_N)$ Pressure drop over a droplet due to the Laplace pressure [N/m^2]
Δp_G Pressure drop due to viscous flow through a gutter [N/m^2]
δ Dimensionless width of the droplet filament
ε Dimensionless length of the droplet filament
Θ The area under the neck measured from an image [m^2]
$\theta = a\omega \approx \Theta/HW^2$ The dimensionless area under the neck shape
κ The dimensionless coefficient represents the average changes in necking flow rate due to the variation of the gutter geometry and droplet curvature
κ_0 The dimensionless coefficient describing the relation between the initial droplet/gutter length and the capillary number
Λ The coefficients of the length dimension characterizing the geometry-dependent shear magnitude in the direction perpendicular to the main channel axis [m]
$\lambda = \Lambda/W$ Dimensionless Λ
λ_0 A constant parameter represents the value of the initial droplet length, l_0, at the higher Ca regime
μ_C The dynamic viscosity of the continuous phase [Pa s].
Ξ The coefficients of the length dimension characterizing the geometry-dependent shear magnitude in the direction along the main channel axis [m]
$\xi = \Xi/W$ Dimensionless Ξ
ρ The dimensionless volume of the droplet filament
ρ_0 The initial dimensionless volume of the droplet filament
π Mathematical constant ≈ 3.14
τ Duration of the necking stage [s]
$\tau^* = \tau Q_C/W^2H$ Dimensionless duration of the necking stage
τ^*_{HL} Dimensionless time when q_N reaches 0.5
$\tilde{\tau} = t\gamma/\mu_C W$ Dimensionless time related to the relaxation experiment
χ A dimensionless coefficient represents the strength of neck-shape elongation
ψ The slope of a versus ω, $da/d\omega$
Ω Time-dependent factor scaling the shape of the neck in the direction along the main channel axis [m]
$\omega = \Omega/W$ Dimensionless Ω
ω_0 Dimensionless Ω at the initial necking or relaxation process
$\langle \cdot \rangle = \frac{1}{\tau}\int_{t=0}^{t=\tau} \cdot\, dt$ Time-average of a quantity $\{\cdot\}$ over the necking stage duration

Subscript and superscript

0 A quantity at the beginning of the necking stage $t = 0$
* Denotes dimensionless time
B Bypass
C Continuous phase
D Droplet phase
G Gutter
HL A quantity at the time when q_N reaches 0.5
L Laplace pressure
N Necking
N0 A quantity at the end of necking stage $t = \tau$
T Tip of the droplet
T0 Tip of the droplet at the beginning of the necking stage $t = 0$

Abbreviations

CP Continuous phase
DP Droplet phase

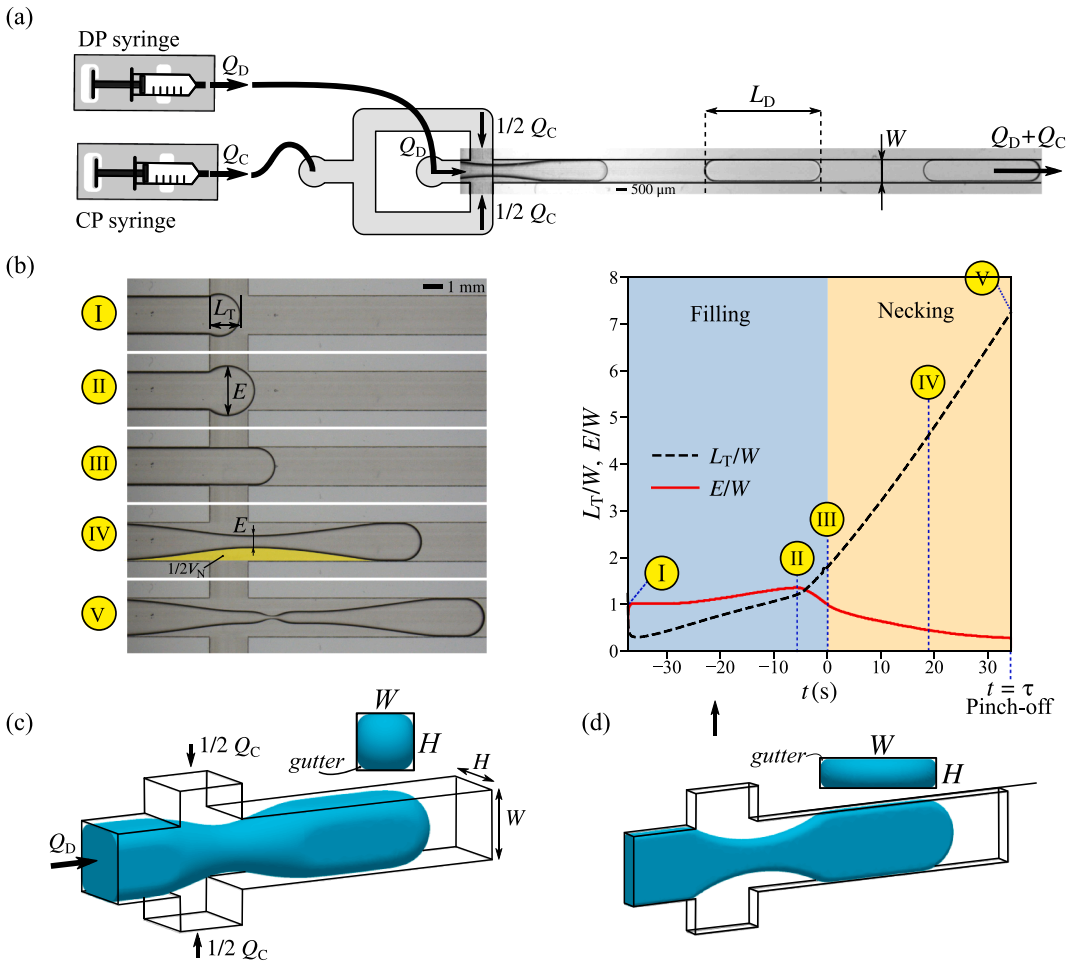

Fig. 1. Formation of droplets in a microfluidic cross-junction. (a) An experimental photo of the formation of a droplet in a cross-junction is displayed as part of a sketch of the experimental setup that features two separate syringe pumps to supply the liquids at constant flow rates. (b) Snapshots showing one droplet formation cycle: the droplet phase fills the junction (I-II), obstructing the flow of the continuous phase. When the width of the forming droplet E is approximately equal to the width of the main channel W(III), marking the start of the necking stage ($\tau = 0$), the continuous phase squeezes the interface, leading to the formation of a neck (IV) that connects the front of the droplet to the feed channel of the droplet phase until it reaches a critical shape (V) at which it breaks ($t = \tau$). This neck is characterized by the volume V_N collected behind it. The corresponding graph on the right shows the evolution of the width E and length L_T of the forming droplet, as defined in Images I, II, and IV, with the filling stage displayed in blue and the necking stage displayed in orange. Snapshots and graphs in (b) were obtained in a device with an aspect ratio $W/H = 4.07$. (c-d) Images of the three-dimensional neck of a forming droplet in a microchannel with a rectangular cross-section with aspect ratios of (c) $W/H = 1$ and (d) $W/H = 4$. The gutters around the forming droplet in the corners of the main channel are best seen from the front view of the droplet. (For interpretation of the references to colour in this figure legend, the reader is referred to the web version of this article.)

led to the following widely accepted classification: At low Ca, when interfacial forces dominate over viscous forces, droplets form at the junction through the "squeezing" mechanism [20–22], with the resulting droplets having a volume larger than that of the junction. At intermediate Ca, when interfacial and viscous forces both play a role, droplets form either directly at the junction, known as "dripping" [20], or further downstream, known as "jetting" [19,20], with the resulting droplets having a volume comparable to or smaller than that of the junction. At high Ca, when viscous forces dominate over interfacial forces, a stable thread forms that extends from the junction all the way to the exit of the device without breaking up into droplets, known as "parallel flow" [23], "tubing" [19], "annular flow" [24], or "threading" [25].

The volume of the droplets thus stems from the interplay between interfacial and viscous forces and hence depends on fluid properties and flow conditions for a given junction geometry [26]. The exception is the squeezing regime, which is unique to the physical confinement in microfluidic systems. In this regime, the volume of droplets primarily depends on the ratio of the flow rates of the two liquids and hardly on Ca. This can be understood by reviewing the droplet formation mechanism in the squeezing regime. In the filling stage, the droplet phase (DP) fills up the junction at a rate of flow Q_D, as illustrated in Fig. 1b (Images I – II), obstructing the channel lumen normally available for the continuous phase (CP) flow. As the CP has its own pressure head and is continually fed at a flow rate Q_C, the emergence of an obstruction in the channel causes the pressure upstream of the forming droplet to increase. In the subsequent necking stage, which starts when the width E of the forming droplet equals the width W of the main channel (Image III), the CP gradually 'squeezes' the DP until the neck reaches a critical shape (Image V) and rapidly breaks, releasing the droplet into the main channel. In this two-stage description, the final droplet volume V_D simply follows from the sum of the volume of the forming droplet at the end of the filling stage V_0 and the volume of the DP added to the forming droplet at a rate Q_D over the duration τ of the necking stage, i.e., $V_D = V_0 + \tau Q_D$. The following three assumptions are critical to translating this relation into the renowned squeezing law [27]:

1. The volume V_0 of the forming droplet at the end of the filling stage is insensitive to fluid properties and flow conditions.
2. The shape of the neck at the end of the necking stage and the corresponding volume V_{N0} of the CP collected behind the forming droplet is insensitive to fluid properties and flow conditions.
3. All of the CP fed at a rate Q_C over the duration τ of the necking stage collects behind the forming droplet and hence contributes to filling the volume V_{NO} such that the duration of the necking stage follows from $V_{NO} = \tau Q_C$.

Under these three assumptions, the classical squeezing law is obtained, i.e., the linear relation between the volume of the droplets and the ratio of flow rates $q = Q_D/Q_C$:

$$V_D = V_0 + V_{NO} q \tag{1}$$

In the classical squeezing model, the droplet volume depends on the value of Ca only through the magnitude of the flow rate. In this work, we defined the capillary number as $Ca = \mu_C U_C/\gamma = \mu_C Q_C/\gamma HW$, where γ is the interfacial tension, H the height of the channel, μ_C and U_C are the dynamic viscosity and the mean speed of the CP, respectively. Thus, when q is constant, the droplet volume is constant and independent of the values of viscosity and interfacial tension. This is true only in a limited range of Ca, as demonstrated originally in T-junction devices [27], flow-focusing devices [20], and cross-junction devices [28,29]. At very low values of Ca, the system behavior diverges from the squeezing regime. It has been shown previously by the experimental results of Cubaud and Mason [19], which include measurements at a very low value of Ca ($< 10^{-3}$), that there is a different droplet formation regime at the lower Ca values, which shows that the droplet volume strongly depends on Ca, i.e., $V_D \propto Ca^{-1}$. Above this regime, their experimental result shows an almost negligible Ca dependency, i.e., $V_D \propto Ca^{-0.17}$, a sign of squeezing regime droplet formation. Indeed, there have been many reports that show the droplet volume in the squeezing regime being dependent on Ca with the proposed modification of Eq. (1) with a scaling to Ca. The common form of the proposed modification comes in the form of $V_D \propto c_1 + c_2 q^k Ca^{-n}$, where c_1, c_2, k, and n are constant parameters obtained from the curve fitting of the experimental/numerical results [30–33]. In general, the reported values of k are approximately unity (1–1.2), whereas the values of n vary; however, they remain less than 0.3. The low value of n renders a weak Ca dependency because most of those results were based on measurements in the higher Ca range, i.e., the squeezing regime or upper regime. Nevertheless, these propositions do not provide an explanatory model of the formation of droplets outside the squeezing regime and do not provide mechanistic insight into why droplet formation becomes strongly dependent on Ca at very low values of Ca.

In recent work [34], we revealed that there is a limit to the validity of the third assumption and hence to the classical squeezing law. For values of Ca of approximately 10^{-4}, an order of magnitude smaller than those typically considered in the literature, we found that the CP fills the volume behind the neck, V_N, at a rate $Q_N (< Q_C)$ and simultaneously leaks around the forming droplet at a nonnegligible rate $Q_B = Q_C - Q_N$. This leaky flow occurs in the so-called gutters [26] in the corners of a rectangular channel, given that the interfacial tension does not permit the interface to conform to the sharp corners (see Fig. 1c/d). The flow rate through the gutters was found to be governed by the balance between interfacial and viscous forces over the gutters, introducing both a time and a Ca dependency into Q_B and, in turn, into Q_N. This subsequently introduces a Ca dependency into the duration τ of the necking stage through $V_{NO} = \tau \langle Q_N \rangle$, with $\langle Q_N \rangle$ being the flow rate of the CP contributing to squeezing of the neck, time-averaged over the duration of the necking stage. Taking this insight into account by altering the third assumption used to arrive at the classical squeezing law (Eq. (1)), we generalized the classical squeezing law to

$$V_D = V_0 + V_{NO} \frac{1}{\langle q_N \rangle} q, \tag{2}$$

with $\langle q_N \rangle = \langle Q_N \rangle / Q_C$ as the (unknown) fraction of the CP contributing to squeezing of the neck, time-averaged throughout the necking stage. Using the characteristic volume W^2H – the volume of the junction or the volume of a channel segment with the length W, this generalized squeezing law can be written in dimensionless form as

$$l_D = l_0 + \nu_{NO} \frac{1}{\langle q_N \rangle} q = l_0 + \tau^* q, \tag{3}$$

where the volumes in Eq. (2) were normalized with the characteristic volume. Note that the term l_0 can be seen as the dimensionless droplet volume at the start of the necking stage. Defining the characteristic time as W^2H/Q_C, i.e., the time needed to fill the volume W^2H by the CP at a flow rate Q_C, we can write τ in dimensionless form as follows: $\tau^* = \tau \frac{Q_C}{W^2H} = \left(\frac{V_{N0}}{\langle Q_N \rangle}\right) \frac{Q_C}{W^2H} = \nu_{NO} \frac{1}{\langle q_N \rangle}$. Thus, the term $\nu_{NO}/\langle q_N \rangle$ in Eq. (3) can be seen as the dimensionless duration of necking stage τ^*.

For T-junctions considered in our previous work [34], we found that the droplet volume at the start of the necking stage as well as the neck shape at the end of the necking stage were the same for the lowest range of Ca numbers, thereby confirming the first and second assumption of the classical squeezing law that V_0 and V_{NO}, and hence l_0 and ν_{NO}, are insensitive to Ca. In addition, we derived that the fraction $\langle q_N \rangle$ takes the functional form $\langle q_N \rangle^{-1} = 1 + \beta/q\text{Ca}$, with β as a parameter depending solely on the aspect ratio of the main channel. The obtained squeezing law for T-junctions ($l_D = l_0 + \nu_{NO} q(1 + \beta/q\text{Ca})$) was found to be in excellent agreement with experiments and allowed us to highlight two essential aspects of droplet formation at low Ca: (i) for $\text{Ca} \gg \beta/q$, the fraction $\langle q_N \rangle$ is approximately one and thus insensitive to Ca, and so is l_D, retrieving the classical form of the generalized squeezing law; (ii) for lower Ca, the fraction $\langle q_N \rangle$ is sensitive to Ca, and so is l_D, showing that there is a lower limit to the squeezing regime, below which the droplet volume depends on fluid properties and flow conditions, i.e., on Ca, as is the case for the dripping and jetting regimes. This new regime, observed at the lowest Ca, was coined the "leaking regime" based on the mechanistic insight that a nonnegligible amount of the CP flows around the forming droplet that acts as a 'leaky' piston [35] inside a channel with a rectangular cross-section.

An open question that remains to be explored is to what extent the generalized squeezing law (Eq. (3)) and the corresponding assumptions on the (in)sensitivity of its parameters on fluid properties and flow conditions apply to droplet formation at low Ca in geometries other than a T-junction, such as in a cross-junction. A notable difference between droplets forming in a T-junction and in a cross-junction is the extent to which the geometry of the junction constrains the neck. In T-junctions, the neck is fully constrained by the walls of the side channel from which the DP is supplied and the walls of the main channel, taking the shape of a quarter of a circle (or elbow) that is uniquely defined by the amount of CP collected behind the neck in the leaking and squeezing regime. In cross-junctions, the neck is not constrained by the walls of the side channels and, to a limited extent, by the walls of the main channel. Therefore, we anticipate that the neck shape in cross-junctions is not uniquely defined by the amount of CP collected behind the neck. We hypothesize that the fundamental difference arising from this difference in constraints on the neck not only leads to a slight quantitative difference in the value of the dimensionless volume ν_{NO} but also to a considerable qualitative difference in the scaling behavior of this parameter that may depend on fluid properties and flow conditions and hence on Ca. In close connection, as the constraints influence the droplet shape prior to pinch-off, they may also affect the filling stage, resulting in a possible Ca dependency in l_0. Finally, the neck shape determines the driving forces for the flow through the gutters, such that we hypothesize that the functional form of the fraction $\langle q_N \rangle$ that contributes to

Table 1
Dimensions and type of cross-junction device. All measurements have a maximum error of ±5μm.

Microchannel cross-section	Width W [μm]	Height H [μm]	Aspect Ratio W/H [-]
Rectangular	2010	494	4.07
Rectangular	1510	495	3.05
Rectangular	955	469	2.04
Rectangular	752	525	1.43
Rectangular	501	525	0.95
Circular	Diameter: 400 μm		

squeezing of the neck is also different between T-junctions and cross-junctions.

This work studies droplet formation in cross-junctions at Ca values significantly lower than those commonly reported. We show the existence of the leaking regime as the squeezing regime lower boundary. In contrast to the generalized squeezing law for T-junctions, where the Ca dependency comes from $\langle q_N \rangle$, here, we show not only that the functional form of $\langle q_N \rangle$ is different in cross-junctions but also that additional Ca dependencies are introduced in l_0 and v_{N0}. After experimentally showing the dependencies and theoretically rationalizing them, we show that the generalized squeezing law (Eq. (3)) is in excellent agreement with our experiments in cross-junctions.

2. Materials and methods

2.1. Device fabrication and the experimental setup

Microfluidic devices were fabricated from polycarbonate (PC) plates (Macrolon, Bayer, Germany). The channels were milled in the plates using a CNC milling machine (Ergwind, Poland), which has a positioning reproducibility of 5 μm. Two identical channels were milled in two PC plates, the depth of each being half of the depth of the channel obtained after bonding the two halves. Bonding was performed using a hot press at 135 °C for at least 12 min. While the PC surfaces are flat after milling, they may deform during bonding. Therefore, we inspected the devices after bonding, using only those without deformations in cross-sectional shape. We fabricated five devices with varying rectangular channel cross-section aspect ratios (see Table 1). In addition, we fabricated a device with a channel with a circular cross-section. After fabrication, no surface modifications were introduced in the channels.

Hexadecane 95% (Sigma Aldrich Co.) and fluorinated oil FC-40 (3 M, USA) were used as the CP and DP liquids, respectively. We chose this combination of working fluids as our model system because it ensures that the CP wets the PC channels thoroughly without adding a surfactant. Effects due to spatiotemporal variations in the surfactant concentration were hence excluded. The viscosities of hexadecane and FC-40 were measured using a falling ball viscometer at 21 °C and found to be $\mu_C = 3.6$ mPas and $\mu_D = 4.1$ mPas, respectively. The interfacial tension between FC-40 and hexadecane was measured using the pendant drop method at 21 °C and found to be $\gamma = 7.3\,\mathrm{mN/m}$.

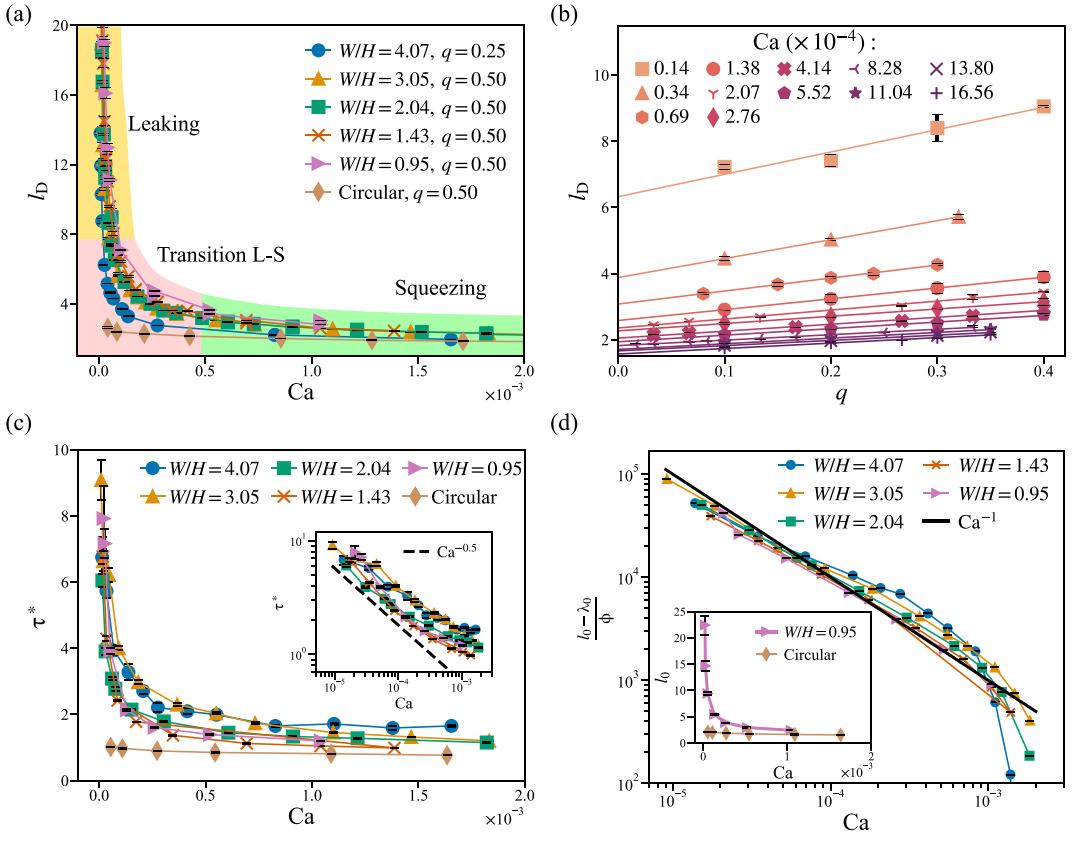

Fig. 2. (a) l_D as a function of Ca for fixed values of q for all devices. The green, pink, and yellow background colors represent the approximate different flow regimes: squeezing, transition, and leaking, respectively. (b) l_D as a function of q for fixed values of Ca in the shallowest device ($W/H = 4.07$), showing that each series with a constant Ca is a linear function of q, per Eq. (3). (c) τ^* as a function of Ca for all devices. Values of τ^* were obtained from the slope of the linear curves in (b). Inset: log–log plot, with the dashed black line indicating $\tau^* \propto Ca^{-0.5}$. (d) Master plot for the leakage term $(l_0 - \lambda_0)/\phi$ as a function of Ca for all devices. Values of l_0 were obtained from the intercept of the linear curves in (b). Coefficients λ_0 and ϕ were estimated for each device separately by fitting the equation $l_0 = \lambda_0 + \phi/Ca$. The solid black line indicates Ca^{-1}. Inset: Comparison between l_0 measured in the circular and rectangular channels ($W/H = 0.95$), showing the Ca independence in the circular channel. (For interpretation of the references to colour in this figure legend, the reader is referred to the web version of this article.)

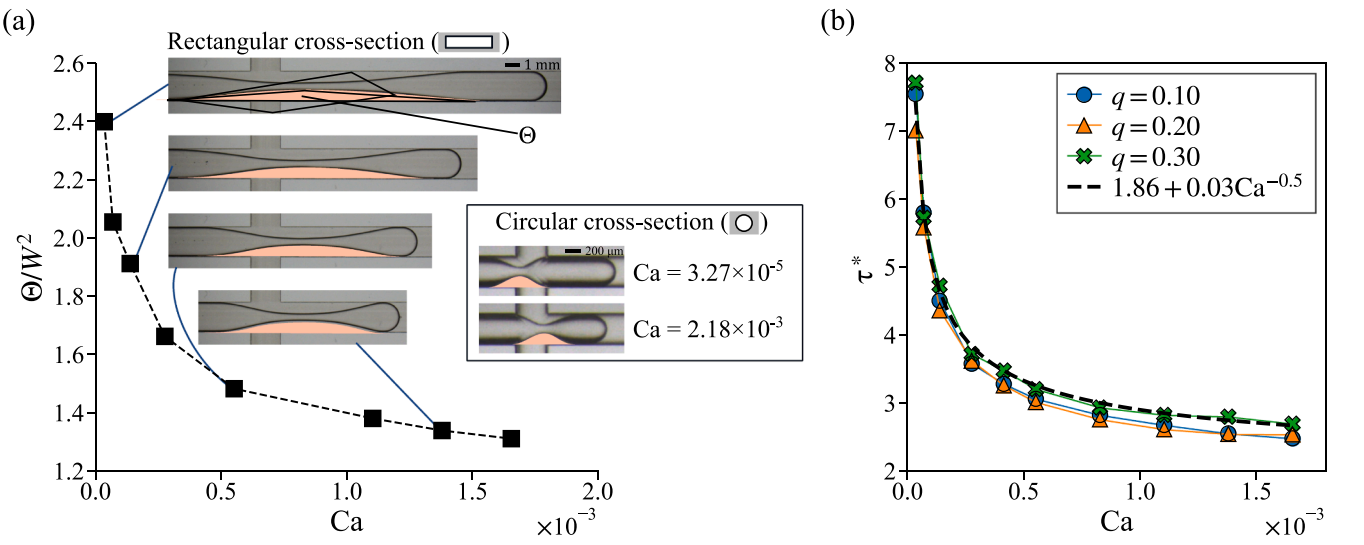

Fig. 3. (a) Critical interface shape prior to pinch-off for different values of Ca. The highlighted area Θ indicates the CP volume collected behind the droplet before pinch-off occurs. This area increases with decreasing Ca. Data were taken in the shallowest device ($W/H = 4.07$) at a fixed ratio of flow rates $q = 0.3$. Inset: critical interface shape observed in the circular cross-section device with two values of Ca that differ by almost two orders of magnitude, showing that the areas Θ are nearly the same. (b) The dimensionless duration of the necking stage as a function of Ca. The values of τ^* were obtained by measuring τ and making it dimensionless through $\tau^* = \tau Q_c/HW^2$. The dashed line is the fitting result that shows $\tau^* \propto Ca^{-0.5}$.

The working fluids were supplied using separate syringe pumps (Cetoni GmbH, Germany) loaded with 1 ml glass syringes (ILS, Germany). We performed additional tests for the lowest flow rates to ensure that in the range of parameters investigated in our research there were no flow fluctuations that the mechanical components of the pumps may generate [36]. The syringes were connected to the inlets of the devices via PE-60 tubing (Beckton-Dickinson, USA). The same tubing was used to connect the outlet of the devices to a waste container. In this study, the range of the flow rate is between 0.01 ml/h and 14 ml/h, covering a Ca range between 7×10^{-6} and 5×10^{-3}. For the complete range of flow rates for each device that we used in this study, we provide a droplet-formation regime map, as shown in Appendix 1.

To ensure the repeatability of the experiments, experiments were performed in a room with the temperature controlled at 21 °C. As reported previously, we noticed that the device orientation affects droplet formation in the low Ca range [37]. Therefore, in each experiment, the horizontal level of the microfluidic device was examined using a digital angle gauge (Limit Level box, Sweden) and maintained within an angle of 0.2°.

2.2. Image acquisition and analysis

The formation of droplets was observed under a stereomicroscope (Zeiss Stemi 508, Germany) equipped with a CCD camera (IDS UI-3274LE-C-HQ, Germany). The recorded images were analyzed using a Python 3 script with various libraries that facilitate numerical image analysis [38,39]. In brief, we obtained the outer profile of the interface of the forming droplets by removing the image background from the original images and converting the resulting images into binary images through thresholding. All the parameters presented in this paper were measured from binary images. Data analysis and curve fitting were performed using the Scipy [40] and Lmfit [41] libraries. Finally, data visualization was performed using the Matplotlib [42] and CMasher [43] libraries.

3. Results and discussion

3.1. Observation of the lower limit of the squeezing regime in cross-junctions

We performed experiments measuring the dimensionless length of the produced droplets l_D for a fixed ratio of flow rates q while varying Ca down to values of 10^{-6}, i.e., much lower than the typical Ca values reported in the literature. For the upper part of the studied Ca range, we confirm that droplets form according to the squeezing regime, with their length being independent of Ca, as illustrated by the green area in Fig. 2a. In sharp contrast, we find that their length does strongly depend on Ca for the lower part of the studied Ca range, as illustrated by the yellow and pink areas in Fig. 2a. This is in line with earlier observations by Cubaud et al. [19] and shows that there is a lower limit to the squeezing regime. The observation that the strong Ca dependence in droplet length is not observed in cross-junctions with a circular cross-section in which gutters are absent (see the diamonds in Fig. 2a) suggests that leaking through the gutters plays a role in droplet formation in cross-junctions. While we, therefore, use the same name, "leaking regime", as previously coined for T-junctions, we do note that the mechanisms at play in this leaking regime are different from those at play in T-junctions; as shown later, there is an additional mechanism in cross-junctions due to fewer geometrical constraints on the neck that introduces additional Ca dependencies to the parameters in the generalized squeezing law in Eq. (3).

Our initial observations suggest that we can describe droplet formation with Eq. (3) as long as we consider both parameters, the dimensionless duration of the necking stage τ^* and the dimensionless initial droplet volume l_0, to be Ca dependent. To test this, we measured l_D as a function of q while fixing Ca. We constructed such curves for different Ca. For each curve, according to Eq. (3), l_D is a linear function of q, with slope τ^* and intercept l_0. Our experimental data are in line with this prediction: l_D is approximately linear in q for all individual curves, as shown in Fig. 2b. Comparing the obtained slope and intercept for all individual curves hence provides a means to separately quantify τ^* and l_0 dependencies on Ca.

We find that τ^* – estimated as the slope of each curve of l_D versus q in Fig. 2b – increases with decreasing Ca, as shown in Fig. 2c. Initial fittings

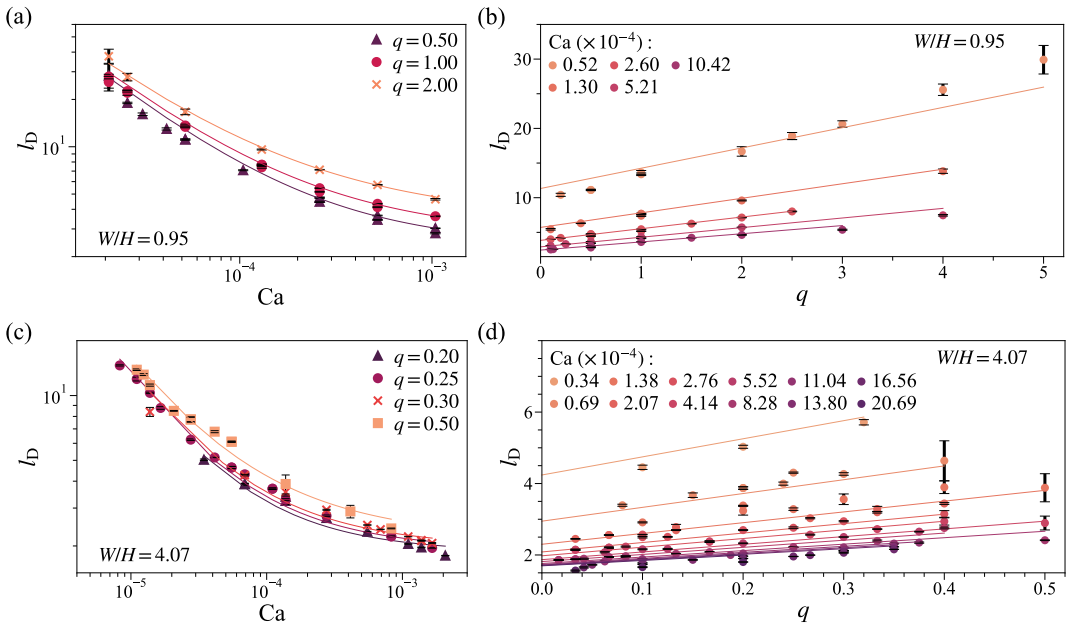

Fig. 4. Comparison between measurements (points) and theoretical predictions (Eq. (4), solid lines) for devices with W/H: (a-b) 0.95; (c-d) 4.07. The (dimensionless) fitting parameters for the two devices are: $W/H = 0.95$: $\chi = 1.62 \times 10^{-2}$, $p = 0.68$, $\lambda_0 = 1.98$, $\phi = 4.87 \times 10^{-4}$; $W/H = 4.07$: $\chi = 2.41 \times 10^{-2}$, $p = 0.97$, $\lambda_0 = 1.65$, $\phi = 0.89 \times 10^{-4}$.

show that $\tau^* \propto Ca^{-n}$ with $n \approx 0.5$ in all cross-junctions with rectangular channels, as shown in the inset of Fig. 2c. By sharp contrast, the Ca dependence of τ^* is almost absent for the junction with circular channels, i.e., the circular cross-section does not permit leaking.

We furthermore find that l_0 – estimated as the intercept of each curve of l_D versus q in Fig. 2b – also increases with decreasing Ca, as shown in the inset of Fig. 2c. Based on initial fitting, we guessed the Ca dependence of l_0 as $l_0(Ca) = \lambda_0 + \phi/Ca$, with λ_0 and ϕ assumed to be independent of Ca and q. However, they may depend on the aspect ratio W/H. We determined their values for the different devices by fitting $l_0(Ca)$ versus Ca for each device separately with the fit function $l_0(Ca) = \lambda_0 + \phi/Ca$. Using the fit values for the different devices, we evaluated the expression $(l_0(Ca) - \lambda_0)/\phi$ for all data series. A master plot of $(l_0(Ca) - \lambda_0)/\phi$ versus Ca is presented in Fig. 2d for all data series, showing that all datasets approximately collapse onto the line $\sim Ca^{-1}$. In the theoretical analysis in Section 3.4.4, we argue that this Ca dependence of l_0 is due to the leaking mechanism, which is most efficient at the filling-necking transition and then gradually diminishes. For comparison, we evaluated l_0 for the junction with circular channels. As expected, this term is independent of Ca, as shown in the inset of Fig. 2d.

3.2. Ca dependency in the final neck shape and the duration of the necking stage at low Ca

The observed Ca dependence in the dimensionless duration of the necking stage, $\tau^* (= v_{N0}/\langle q_N \rangle)$, may have two origins: (i) the possible Ca dependence of the neck shape and hence of the dimensionless volume of the CP collected behind the forming droplet at pinch-off ($v_{N0}(Ca)$) and (ii) the possible Ca dependence of the fraction of the CP contributing to the squeezing of the interface ($\langle q_N \rangle(Ca)$). We studied these dependencies separately for v_{N0} and τ^* by observing the microscope images.

To quantify the Ca dependence of $v_{N0}(Ca)$, we analyzed the images prior to pinch-off. We find that the critical interface shape does depend on Ca, as evident from the snapshots presented in Fig. 3a. For decreasing values of Ca, the neck extends further into the main channel, both in the upstream and downstream directions. Additionally, we compare the images prior to pinch-off with those recorded in the circular channel. While the Ca values of the two presented images for the circular channel differ by almost two orders of magnitude, the volume of CP collected behind the neck is comparable, albeit with a different breaking location of the neck (see the inset of Fig. 3a). To further quantify the Ca dependence of $v_{N0}(Ca)$, we measured the area Θ from the two-dimensional images. We find that this area increases with decreasing Ca, as shown in Fig. 3a.

To quantify the Ca dependence of τ^*, we analyzed the duration of the necking stage based on the images, with the start and end of the necking stage defined as $E/W(t = 0) = 1$ and $E/W(t = \tau) = 0$, respectively. The measurements of τ^* show a strong Ca dependency for the lower values of Ca and a weak dependence on q for the whole range of Ca, as shown in Fig. 3b. A fit shows a proportionality close to $Ca^{-0.5}$, in good agreement with the Ca dependency obtained in the less direct way through fitting l_D versus q curves, as shown in the inset of Fig. 2c.

3.3. Generalized squeezing law

We have seen that the generalized squeezing law (Eq. (3)) describes the formation of droplets in cross-junctions at low Ca, but with the notion that, unlike in T-junctions, the parameters $\langle q_N \rangle$, v_{N0}, and l_0 are all Ca dependent. While the Ca dependency in $\langle q_N \rangle$ originates from the CP flowing around the forming droplet, the Ca dependency in v_{N0} and l_0 both originate from the flow-dependent shape of the neck, which is less constrained in cross-junctions than in T-junctions. Including the observed Ca dependencies, the generalized squeezing law for cross-junctions takes the form

$$l_D = \lambda_0 + \frac{\phi}{Ca} + q\left(\frac{\chi}{\sqrt{Ca}} + p\right). \tag{4}$$

The first and second terms on the right-hand side come from the replacement of l_0 in Eq. (3) by the Ca-dependent term $\lambda_0 + \phi/Ca$ introduced above and justified in the following sections. The third term includes the observed Ca dependency of the duration of the necking stage. The parameters λ_0, χ, p, and ϕ do not depend on Ca but may depend on the aspect ratio of the rectangular channels of the cross-junction. For higher Ca values ($Ca > 10^{-3}$), Eq. (4) returns the classical squeezing law. The functional form is in good agreement with the experimental data, as illustrated in Fig. 4 for all data series obtained in the junctions with

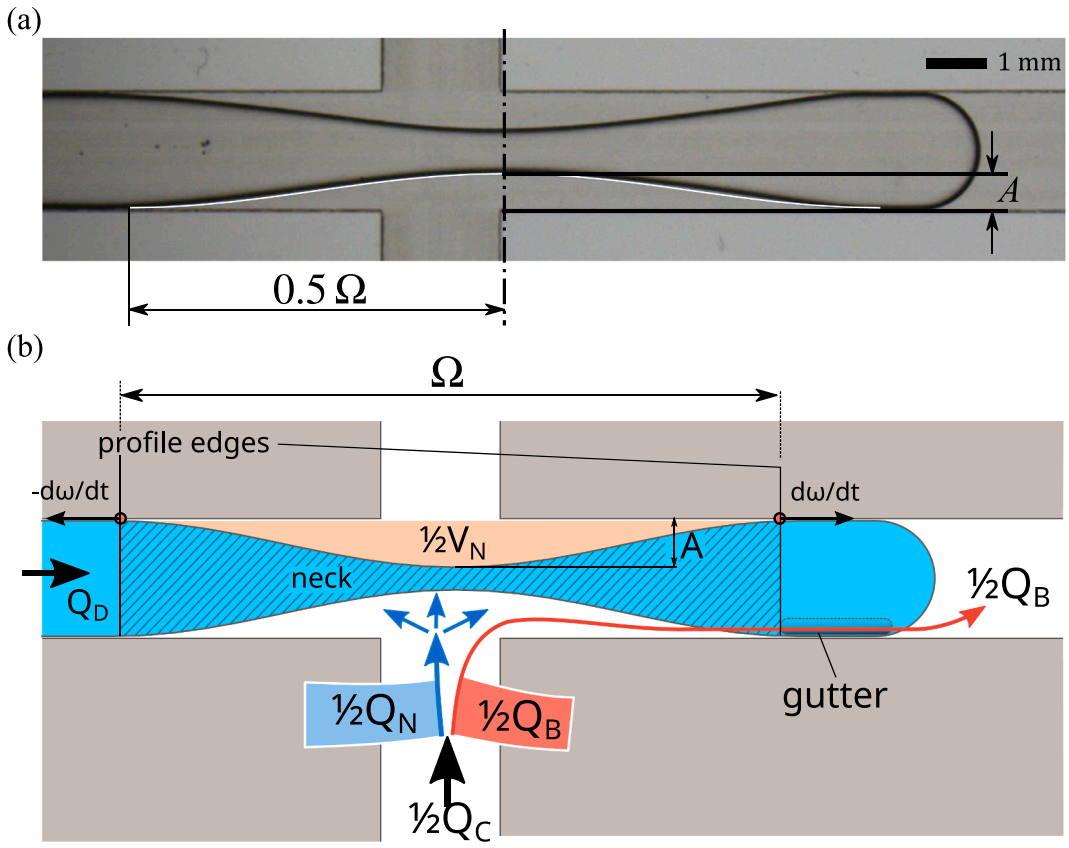

Fig. 5. (a) The neck of a forming droplet, as seen from a top-view image, takes the shape of part of a sine wave, with amplitude $A/2$ and wavelength Ω, as evident from the overlay of this shape (white line) on a prototypical image. The image was taken in the device with $W/H = 4.07$, during necking with $\mathrm{Ca} = 1.38 \times 10^{-4}$ and $q = 0.3$. (b) A schematic of droplet formation that depicts the balance of the flow rate and the balance of forces. As the DP fills the forming droplet at a rate Q_D, part of the incoming CP accumulates behind the neck, filling the volume V_N at a rate Q_N. The remainder of the incoming CP flows around the forming droplet through the gutters at a rate Q_B. During necking, the neck width increases at a rate of $d\omega/dt$ as a result of the interplay between interfacial and viscous forces.

rectangular channels of aspect ratio $W/H = 0.95$ and 4.07. Other experimental results using other aspect ratio devices and liquid pair are shown in Appendix 2 and Supplementary Note 3, respectively.

Some previously reported measurements have shown similar behavior at low Ca as in the current study. For example, the experimental result of Cubaud and Mason [18] show two different droplet formation regimes. The two regimes were distinguished based on the threshold value of $l_D \approx 2.5$ [18,29]. For $l_D > 2.5$, l_D increases by proportionality $\propto \mathrm{Ca}^{-1}$ [18]. This result can be readily explained by the leaking mechanism that we described here; for example, Eq. (4) shows the proportionality of $l_D \propto \mathrm{Ca}^{-1}$ and thus confirms the leaking regime. Furthermore, we can determine the leaking regime boundary based on the dimensionless parameter ϕ in Eq. (4). There is no fixed value of ϕ, as this parameter may depend on the device geometry, for example, W/H of the device (see Supplementary Notes 1 and 2). Based on our experimental results (see Figs. 4 and 11), ϕ is typically less than 1×10^{-3}. In the remainder of this article, we will rationalize the Ca dependencies using a theoretical model.

3.4. Theoretical model

We developed a semiempirical model to gain insights into the mechanisms that introduce the dependency of the ratio of flow rates and the capillary number in the dimensionless duration of the squeezing stage (τ^*) in Eq. (3), and hence in the length of droplets produced in cross-junctions in the leaking regime, i.e., at vanishing values of Ca.

As a first simple approximation, we started our analysis based on the experimental data obtained from the device with the highest aspect ratio ($W/H = 4.07$) and assumed the droplet outline as two-dimensional curves (i.e., a flat droplet), neglecting variations in the channel depthwise direction. At a later stage, the result of the flat-droplet analysis is verified by using experimental data from other devices with different aspect ratios. Additionally, the following analysis is restricted to the upper or lower half of the droplet, assuming interface symmetry relative to the main channel middle axis.

3.4.1. Neck profile

In all of our experiments, we observed that the neck of a forming droplet takes the prototypical shape illustrated in Fig. 5. As seen from a top-view image, the two-dimensional profile of the neck appears to take the shape $h(x)$ as part of a sine wave (or cosine), with amplitude $A/2$ and wave length Ω, i.e.,

$$h(x) = 0.5A\left[1 + \cos\left(\frac{2x}{\Omega}\pi\right)\right]. \tag{5}$$

This shape fits the neck profile very well, as seen from the overlay in Fig. 5a. In fact, as we will show later, we observed that this shape not only describes the neck profile over a large portion of the necking stage but that the shape is also self-similar, i.e., the aspect ratio A/Ω is approximately constant over time.

3.4.2. Neck evolution

The instantaneous interface shape of the neck and its evolution stem from a balance between interfacial and viscous forces. Assuming that the out-of-plane interface shape is imposed by the spacing between the top and bottom walls along the entire neck, the interface can only adjust its shape in the in-plane direction visible in the top-view images (see

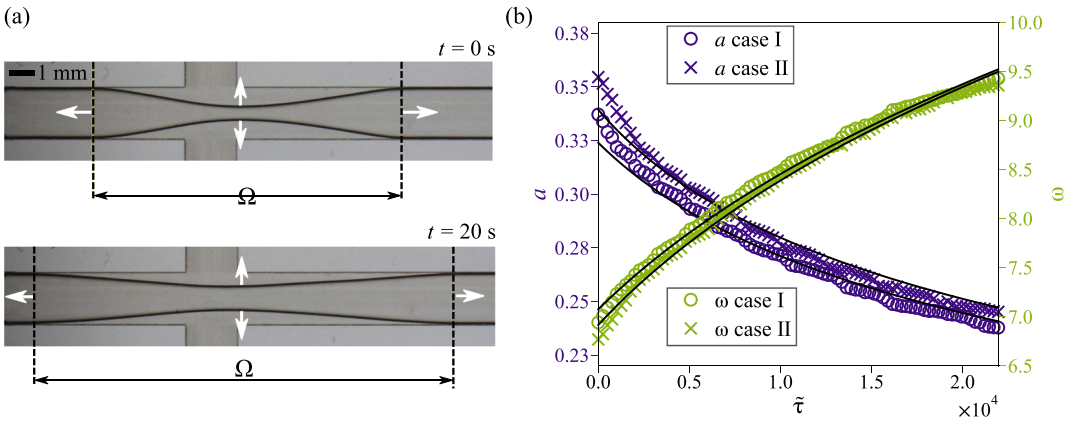

Fig. 6. Experimental verification of the neck evolution equation (Eq. (10)) using stop-flow experiments. First, the outlet channel is filled with DP, and DP flow is stopped. Second, CP is fed with a constant flow rate Q_C. Third, the CP flow is stopped approximately before pinch-off, and the relaxation process is recorded and analyzed. (a) Images of the neck shape immediately after stopping the flow (top) and 20 s later (bottom). (b) Analysis of the relaxation of the neck in terms of the evolution of the amplitude A and the wavelength Ω (both normalized by W). The two presented cases differ in an instant during the formation process when the flow is stopped, i.e., in their initial shape (A_0, ω_0). Black lines correspond to the curve fitting by Eq. (10). Experiments were conducted in the cross-junction device with $W/H = 4.07$. Case I and Case II were obtained by injection of CP with flow rates of 3 ml/h and 4 ml/h, respectively. The fitting results are $\xi = 0.028$, $\lambda_0 = 0.448$, $a_{0\ \text{Case I}} = 0.324$, $\omega_{0\ \text{Case I}} = 7.075$, $a_{0\ \text{Case II}} = 0.339$, and $\omega_{0\ \text{Case II}} = 6.91$.

Fig. 5b). The order of magnitude of the interfacial force associated with the in-plane adjustment follows directly from the interface curvature. The maximum curvature (at the center of the profile $h(x)$) scales with the ratio A/Ω^2. Taking it as a representative value for the order of magnitude of the curvature, the pressure difference along the interface stemming from interface forces is proportional to $\gamma A/\Omega^2$. The order of magnitude of the viscous force follows from considering the flow of the CP in the gap between the interface and the wall. For simplicity, we focus only on two orthogonal directions of the flow: along the main channel (changing Ω) and transverse to it (changing A). The flow velocities in both directions can be approximated by $d\Omega/dt$ and dA/dt, respectively. Furthermore, the contribution to the pressure stemming from viscous forces associated with the motion in the principal directions can be estimated as $\mu_c/\Xi \cdot d\Omega/dt$ and $\mu_c/\Lambda \cdot dA/dt$, respectively, where Ξ and Λ are the coefficients of the length dimension characterizing the geometry-dependent shear magnitude in the two directions. Balancing the pressure contributions, we obtain

$$\frac{\mu_C}{\Xi}\frac{d\Omega}{dt} = \frac{\mu_C}{\Lambda}\frac{dA}{dt} + \gamma\frac{A}{\Omega^2}. \tag{6}$$

To describe how the interface evolves, i.e., how A and Ω simultaneously evolve, we also need the continuity equation, which features the instantaneous volume of the neck V_N and the instantaneous flow rate Q_N with which the neck is filled

$$\frac{dV_N}{dt} = Q_N. \tag{7}$$

To solve $A(t)$, $\Omega(t)$, $V_N(t)$, and $Q_N(t)$, two additional relations are needed. The relation between the amplitude $A(t)$, wavelength $\Omega(t)$, and neck volume $V_N(t)$ straightforwardly follows from the geometry of the neck, $V_N \approx 2H\int_{-\Omega/2}^{\Omega/2} h(x)dx$, where we neglect the curved interface in the depthwise direction for simplicity. Evaluating this integral with the neck profile, we find the third relation

$$V_N \approx HA\Omega. \tag{8}$$

The fourth relation between the four variables above that describe the neck and its evolution, for example, requires further information on the flow rate Q_N or on the (self-similar) neck profile. In case $Q_N \approx Q_C$, a closed form expression for the interface evolution can be derived, as we will see next for a particular case in which the continuous feed flow is stopped during the formation of a droplet, and the relaxation of the interface of the forming droplet is studied under this assumption.

3.4.3. Verification by the stop-flow experiment

To verify the validity of Eqs. (6) – (8) without further knowledge of the neck flow rate or interface profile, we performed preliminary experiments in which we observed the evolution of neck shape in a relaxation process instead of a droplet-formation process. The experiments were performed as follows. First, we filled the whole outlet channel with DP and then stopped the DP flow. Second, we injected the CP at a fixed flow rate to squeeze the DP in the junction, allowing the necking process to be similar to the droplet-formation process. Third, we stopped the CP flow before neck pinch-off, as illustrated by the top image in Fig. 6a, and observed the relaxation of the interface profile over time, as illustrated by the bottom image in Fig. 6a. More precisely, we measured the evolution of $a \equiv A/W$ and $\omega \equiv \Omega/W$ during relaxation for two cases, where initial neck shapes were obtained by injection of CP with flow rates of 3 ml/h and 4 ml/h, respectively.

Given that $Q_C = 0$ after stopping the flow, and the resistance to flow through the gutters is significantly larger than the resistance to flow in the neck region, we expect the CP volume accumulated behind the neck to remain constant during relaxation. Hence, there is no flow of the CP into/out of the neck region, i.e., $Q_N(t) = 0$. This stop-flow experiment hence verifies Eqs. (6) – (8) for the case where the neck volume remains constant over time, $V_N(t) = V_0$. By using $\lambda = \Lambda/W$, $\xi = \Xi/W$, $v_0 = V_0/W^2H = a_0\omega_0 = a\omega$, and $t = \tilde{\tau}\mu_C W/\gamma$, we combine Eqs. (6) – (8) to obtain the following nondimensional equation that describes the evolution of the dimensionless wavelength $\omega(\tilde{\tau})$:

$$\frac{1}{\xi}\frac{d\omega}{d\tilde{\tau}} = -\frac{1}{\lambda}\frac{v_0}{\omega^2}\frac{d\omega}{d\tilde{\tau}} + \frac{v_0}{\omega^3}. \tag{9}$$

Solving it with initial condition $d\omega/d\tilde{\tau}(\tilde{\tau} = 0) = 0$, we obtain

$$\omega(\tilde{\tau}) = \omega_0\sqrt{\sqrt{\left(\frac{a_0}{\omega_0}\frac{\xi}{\lambda}+1\right)^2 + 4\xi\frac{a_0}{\omega_0^3}\tilde{\tau}} - \frac{a_0}{\omega_0}\frac{\xi}{\lambda}}. \tag{10}$$

The stop-flow solution (Eq. (10)) is shown as solid lines in Fig. 6b, describing the evolution of ω and a during the relaxation process very well. Here, we hence confirm the validity of Eqs. (6) – (8) in case $Q_N(t) = 0$, i.e., $V_N(t)$ is constant in time.

3.4.4. Leaking flows through the gutters

During droplet formation, a nonnegligible fraction of the incoming CP may flow around the forming droplet, not contributing to the

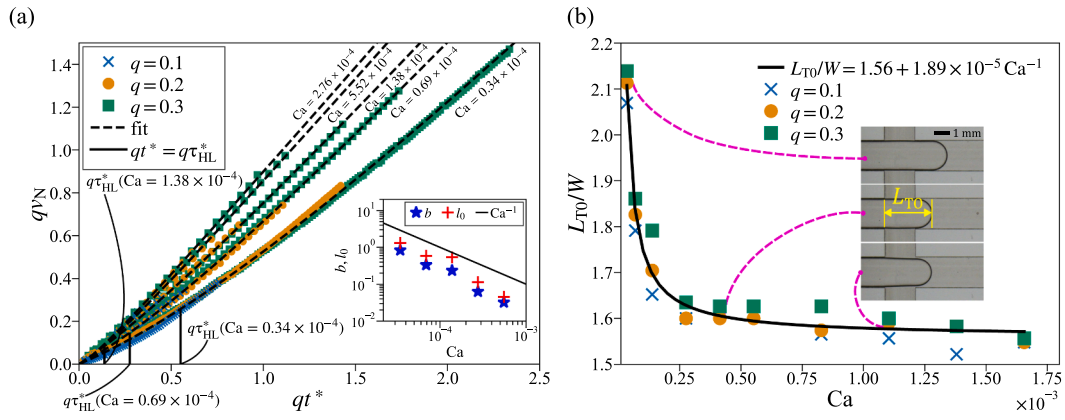

Fig. 7. Experimental analysis of the leaking flow. Values of $v_N = a\omega$, τ^*, and L_{T0} were measured from the images recorded using appropriately high spatial and temporal resolutions. (a) v_N plotted as a function of qv_N versus qt^* for different values of q and Ca. According to Eq. (16), different data series collapse on separate lines, each characterized by a unique Ca. Dashed lines show the curve-fitting result of Eq. (16) with $b = \kappa/\mathrm{Ca}$ and l_0 set as the curve-fitting parameters to the data series with the same Ca. The inset shows the Ca dependency of the fitted parameters b and l_0. The parameters κ and κ_0 were estimated by fitting to experimental point functions $b = \kappa/\mathrm{Ca}$ and $l_0 = \kappa_0/\mathrm{Ca}$, respectively. The fittings provided the values $\kappa = 2.7\times10^{-5}$ and $\kappa_0 = 3.5\times10^{-5}$. Solid vertical lines show the three highest $q\tau^*_{HL}$ values for the three smallest values of Ca, as indicated by the attached labels. (b) Measurement of the droplet tip position (points) relative to the junction at the start of necking, L_{T0}, versus Ca. The solid line is the curve fitting result of L_{T0} as a function of Ca which shows Ca dependency with proportionality of Ca^{-1}. The presented measurements are taken from experiments using the device with aspect ratio $W/H = 4.07$.

squeezing of the neck. Considering the flow through the gutters, we now derive an expression for the flow rate through the gutters and hence for the flow rate Q_N. The resulting expression, together with Eq. (6) – (8), describes the evolution of the neck. This set of model equations can be used to determine an expression for the dimensionless duration of the squeezing stage (τ^*) and its dependencies on Ca and q.

We balance the pressure difference over the gutters due to a difference in curvature, Δp_L, with the pressure difference over the gutters due to viscous flow through the gutters, Δp_G. The curvature at the tip (K_F) is assumed to be constant and imposed by the height and width of the main channel, i.e., $K_F = \frac{2}{H} + \frac{2}{W}$. The curvature at the center of the neck ($x = 0$) is estimated as $K_N = \frac{2}{H} - \frac{\pi^2}{2}\frac{A}{\Omega^2}$, with the in-plane curvature $\pi^2 A/2\Omega^2$ calculated from the neck profile (Eq. 5) as $\partial^2 h/\partial x^2(x = 0)$. The pressure drop across the droplet, neglecting the viscous pressure drop inside the droplet, is

$$\Delta p_L = \frac{\gamma}{W}\left(2 + \frac{\pi^2}{2}\frac{a}{\omega^2}\right). \tag{11}$$

This pressure difference balances the pressure difference due to viscous flow through the gutters. Considering four gutters, the CP flows through each gutter at a rate Q_G ($= Q_B/4$). We assume the gutters to have a constant cross-sectional area A_G and an initial length L_0 that increases over time at a rate Q_D/WH. The pressure difference is described by

$$\Delta p_G = \alpha\mu_C A_G^{-2}\left(L_0 + \frac{Q_D}{WH}t\right)Q_G \tag{12}$$

with α as the cross-section-specific friction factor [44].

By considering $Q_G/Q_C = (Q_C - Q_N)/4Q_C$, $t^* = tQ_C/W^2H$ and normalizing all lengths with W, we write the pressure balance in dimensionless form as

$$2 + \frac{\pi^2}{2}\frac{a}{\omega^2} = \frac{\alpha}{4}\left(\frac{WH}{A_G}\right)^2 \mathrm{Ca}(qt^* + l_0)(1 - q_N), \tag{13}$$

with $q_N = Q_N/Q_C$ being the (dimensionless) fraction of the incoming CP contributing to squeezing of the neck. Note that the gutter area A_G, and hence its dimensionless equivalent A_G/WH, depends on the aspect ratio W/H of the main channel. The solution to Eq. (13) for q_N is:

$$q_N = 1 - \frac{4}{\alpha}\left(\frac{A_G}{WH}\right)^2 \frac{2 + \frac{\pi^2}{2}\frac{a}{\omega^2}}{\mathrm{Ca}(qt^* + l_0)}. \tag{14}$$

Given that the amplitude of the neck shape is generally lower than half of the channel width and the neck width grows from an initial value about the width of the channel, i.e., $\frac{\pi^2}{2}\frac{a}{\omega^2} \ll 2$ (see, for example, a/ω in Fig. 8), we note that the temporal change of q_N primarily follows the extension of the gutter. Replacing the term $\frac{4}{\alpha}\left(\frac{A_G}{WH}\right)^2\left(2 + \frac{\pi^2}{2}\frac{a}{\omega^2}\right)$ with its average value κ, we obtain

$$q_N = 1 - \frac{\kappa}{\mathrm{Ca}(qt^* + l_0)}. \tag{15}$$

The above equation shows that the leaking mechanism in cross-junctions is considerably different than that in T-junctions. Although in both geometries, the flow around the forming droplet through the gutters depends on fluid properties and flow conditions, this dependency manifests in different ways. While in cross junctions, the flow around the forming droplet through the gutters decays over time; in T-junctions, it is time-constant [34].

The (dimensionless) expression for q_N (given in Eq. (15)) together with the dimensional expressions provided earlier (Eq. (6) – (8)) allow describing the evolution of the interface. Alternatively, we can use the definition $v_N(t^*) = \int_0^{t^*} q_N dt^*$, integrate Eq. (15) and then multiply it with q to obtain

$$qv_N = qt^* - \frac{\kappa}{\mathrm{Ca}}\ln\left(\frac{qt^*}{l_0} + 1\right). \tag{16}$$

This approach has a slight advantage over Eq. (15) because the neck area is directly observable in our experiments. To verify Eq. (16), we measured a, ω, and the area under the neck θ during the formation of droplets for various q and Ca values in the device with aspect ratio $W/H = 4.07$ using a higher image resolution and frame rate. The resulting curves (qv_N) are then fitted with Eq. (16), with qt^* as the independent variable and κ and l_0 as the curve-fitting parameters. We find that all curves are well described by Eq. (16), as plotted in Fig. 7a, with a constant value of $\kappa = 2.7\times10^{-5}$, while the values of l_0 are Ca dependent, as shown in the inset of Fig. 7a. More specifically, they are inversely proportional to Ca, i.e., $l_0 = \kappa_0/\mathrm{Ca}$, with $\kappa_0 = 3.5\times10^{-5}$.

After confirming Eq. (16), we now return to Eq. (15) since the

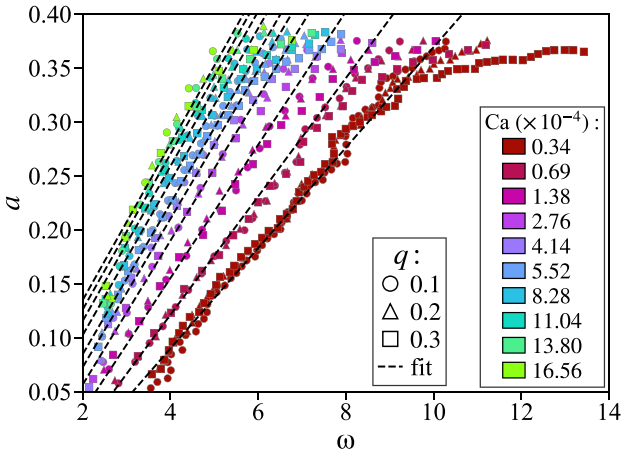

Fig. 8. Neck profile as characterized by the dimensionless amplitude $a = A/W$ versus dimensionless wavelength $\omega = \Omega/W$ during the formation of droplets. Points are measurements taken in the device with aspect ratio $W/H = 4.07$, with different values of q and Ca represented by different marker shapes and colors, respectively. Dashed lines – a plot of the theoretical line: $a = (\omega - \omega_0)\psi$, where ψ is given by Eq.(18). The parameters obtained from the fitting are $\xi/\lambda = 13.56$ and $\xi = 0.023$, with the assumption that $q_N \approx 1$. The fitting of the experimental data revealed that ω_0 is Ca-dependent with the approximated relation $\omega_0 = 11.25\mathrm{Ca}^{-0.13} - 4.91$.

obtained variables immediately provide insight into the fraction of the incoming CP contributing to necking. We define the characteristic dimensionless time of leaking τ^*_{HL}, for which the flow around the forming droplet through the gutters drops to half of its maximal available value so that q_N reaches a value of 0.5: $\tau^*_{HL} = \frac{2\kappa - \kappa_0}{q\mathrm{Ca}}$. For all curves in Fig. 7a, we find that the term τ^*_{HL} is considerably smaller than the duration of the entire necking τ^*. Thus, in further analysis, we assume that beyond the short initial period of necking, the Ca variation of q_N introduced by the second term in Eq. (15) is considerably small, and we can use the simplified approximation $q_N(t^* \gg \tau^*_{HL}) \approx q_N(\tau^*) = q_{N0}$, where q_{N0} is a constant close to unity.

3.4.5. Droplet length at the end of the filling stage

Thus far, we have discussed the mechanisms that give rise to the q and Ca dependency during the necking stage. Since the droplet shape prior to pinch-off is q and Ca dependent, it may be the same case for the dynamics of the filling stage and the droplet length at the end of the filling stage (l_0 in Eq. (3)). Therefore, we also measured the droplet tip position relative to the junction before necking starts (i.e., for $E = W$, see Image III in Fig. 1b), denoted as L_{T0}, as illustrated in Fig. 7b. Although L_{T0} is not a direct measurement of l_0, we expect it to depend on Ca in a similar manner. Fig. 7b shows $L_{T0} \propto \mathrm{Ca}^{-1}$, which shows that the Ca dependency in the measured length of the droplets is introduced not only in the necking stage but also in the filling stage.

3.4.6. Summary of the dependence of l_D on Ca

In the case of the stop-flow experiment, we obtained the solution for ω as a function of time, whereas in the case of necking, the resulting solution would be too complex. Therefore, we developed a semi-empirical solution for the problem by observing the necking process details. Fig. 8 shows the plots of a versus ω for different values of Ca and q.

We divide those data into two regimes, where the delimiter is an arbitrary value of $a = 0.26$. Next, we will analyze the data series and solutions in both regions. Meanwhile, for $a < 0.26$, the experimental points lie on the regular lines, and data for the same Ca collapse on the same line regardless of q. We can also see that these lines' tangent depends on Ca. For $a > 0.26$, we can see that experimental data for different q values separate, and we can expect the dependency on both Ca and q.

Lower regime ($a \leq 0.26$)

For the lower regime ($a \leq 0.26$), we assume that the evolution of the shape is described by Eq. (6) and consider instantaneous q_N as

$$q_N = \frac{d(a\omega)}{dt^*} = a\frac{d\omega}{dt^*} + \omega\frac{da}{dt^*}. \tag{17}$$

Let us assume that the a versus ω relation can be described by linear equation $a = (\omega - \omega_0)\psi$, with ψ being the tangent of the term $\psi = da/d\omega$. In this regime, we may assume that for each Ca, the necking undergoes self-similar shapes, i.e., $\psi \approx a/\omega$, and that it is constant, i.e., $d\psi/d\omega = 0$. Finally, solving Eqs. (6) and (17) under the assumptions mentioned above, we obtain the following:

$$\psi(\mathrm{Ca}) = 2\left(\frac{\xi}{\lambda} + \sqrt{\left(\frac{\xi}{\lambda}\right)^2 + \frac{8\xi}{q_N\mathrm{Ca}}}\right)^{-1}. \tag{18}$$

Fig. 8 shows that the obtained relation describes the Ca dependence of the tangent of the a versus ω relation for experimental data for $a \leq 0.26$.

Eq. (18) requires additional comments, as the time-invariance of the slope $\psi(\mathrm{Ca})$, postulated here and experimentally shown, may cause concern to the careful reader. It contains q_N, which, according to Eq. (15), varies with time. To justify these contradictory statements, we return to the analysis of the gutter flow and its conclusions given in Section 3.4.4. We noted there that even though Eq. (15) introduces the time dependence of q_N, it also shows its relatively rapid stabilization after a short initial period in which it rises to a value close to the final value.

Therefore, for the simplicity of our calculations, we neglect the initial growing period of q_N and assume that for most of the droplet formation process $q_N \approx q_{N0}$, where q_{N0} is a constant close to unity.

Upper regime($a > 0.26$)

Previously, we have shown that the necking of the lower regime can be estimated as a self-similar evolution of the cosine shape, in which we can assume a constant a/ω. Following this self-similar evolution there is a short period of neck elongation in the streamwise direction. In this mode, the cosine shape breaks due to its apex flattening as the thinnest part of the neck elongates. As shown in Fig. 8, for $a > 0.26$, ω grows substantially higher compared to the growth of a. As a increases slowly, eventually, it reaches critical value where the filament breaks, ending the droplet formation process. We call this thin-long neck a filament, shown schematically in Fig. 9a.

Assuming the filament as a box with dimensionless length ε and width δ (see Fig. 9a), the dimensionless volume of the filament is the product of ε and δ, $\rho = \varepsilon\delta$. ρ evolves due to the inflow of DP; therefore, its increment ($\Delta\rho = \rho - \rho_0$, where ρ_0 is the initial volume for $a = 0.26$) is proportional to the product of q and the increment of time: $\Delta\rho \propto q\Delta t^*$. Assuming that ε grows linearly with time, $\Delta\varepsilon \propto \Delta t^*$, we can write ρ as $\rho = cq\Delta\varepsilon + \rho_0$ and obtain the equation for δ as

$$\delta = \frac{\rho_0 + cq\Delta\varepsilon}{\varepsilon}, \tag{19}$$

where c is a constant. Next, we assume ε elongates with the same rate as ω such that $\Delta\varepsilon \approx \Delta\omega$, where $\Delta\varepsilon = \varepsilon - \varepsilon_0$. Finally, we substitute δ into the equation for the evolution of $a = 0.5(1 - \delta)$ and obtain relation a as a function of the increment of the width of the profile $\Delta\omega$:

$$a = 0.5\left(1 - \frac{\rho_0 + cq\Delta\omega}{\Delta\omega + \varepsilon_0}\right). \tag{20}$$

The fitting result of Eq. (20) to the experimental data for $a > 0.26$ is shown in Fig. 9b. From the curve fitting, we obtained the following relation:

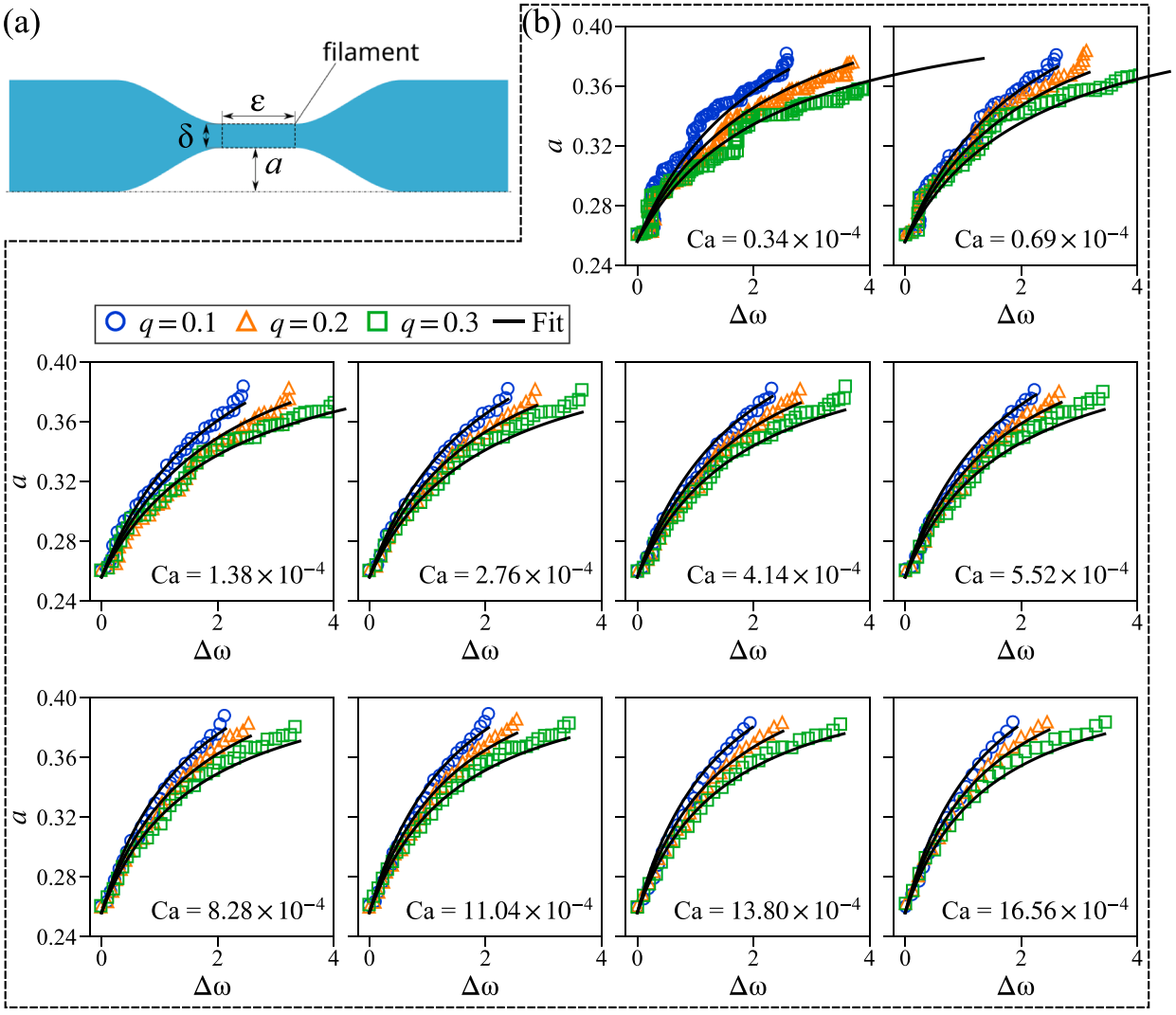

Fig. 9. (a) In the upper regime $a > 0.26$, the increase in filament length ε is faster than the thinning of filament width δ. (b) Kinematics of the filamenting stage. Points are the experimental data for different values of q. The solid lines are the fitting results of Eq. (20) with fitting parameters. $\varepsilon_0 = 1.32 + 2.51 \times 10^{-4}(1.63 \times 10^{-4} + \mathrm{Ca})^{-1}$. Graphs without a y-axis label and numbers have their y-axis shared with the figure on their left. Measurements were taken in the device with $W/H = 4.07$.

$$a = 0.5\left(1 - \frac{0.48\varepsilon_0 + 0.48q\Delta\omega}{\Delta\omega + \varepsilon_0}\right), \tag{21}$$

where $\varepsilon_0 = 1.32 + 2.51 \times 10^{-4}(1.63 \times 10^{-4} + \mathrm{Ca})^{-1}$.

The previous analysis allowed us to identify the additional dependency on parameters τ^* and l_0 of Eq. (3) to the flow rate condition such as Ca. We will include these dependencies to generalize Eq. (3) for the cross-junction device.

We have identified various mechanisms that contribute to the prolongation of τ^*. According to Eq. (16), for $v_N(t^* = \tau^*) = v_{N0}$, we have:

$$\tau^* = v_{N0} + \frac{\kappa}{q\mathrm{Ca}}\ln\left(\frac{q\tau^*}{l_0} + 1\right). \tag{22}$$

Eq. (22) is interesting in its own right. The physical interpretation of this equation is that the (dimensionless) duration of necking is equal to the time needed to fill the volume behind the neck plus the time delay due to leakage of CP through the gutter. In the higher Ca regime, the last term of Eq. (22) vanishes such that $\tau^* = v_{NO}$. Thus, Eq. (22) returns the same τ^* as in the original squeezing model, assuming negligible leaking, i.e., by setting $\langle q_N \rangle = 1$ in Eq. (3).

Let us call the three identified contributions τ_1^*, τ_2^*, and τ_3^*, with $\tau_1^* + \tau_2^* = v_{N0}$ and $\tau_3^* = \frac{\kappa}{q\mathrm{Ca}}\ln\left(\frac{q\tau^*}{l_0} + 1\right)$, such that $\tau^* = \tau_1^* + \tau_2^* + \tau_3^*$. In the first term, τ_1^* is taken from the elongation of the sinusoidal shape of the neck in the lower necking regime. According to Eq. (18), we can write the instantaneous volume under the neck as $v_N = \frac{a^2}{\psi} = a^2\left(\sqrt{\left(\frac{\xi}{\lambda}\right)^2 + \frac{8\xi}{q_N\mathrm{Ca}}} + \frac{\xi}{\lambda}\right)$. At the end of the lower regime of necking $v_N(a \approx 0.26)$, for simplicity, we assume q_N reaches its asymptotic value, which is equal to 1 (Eq. (15)). This leads to $\tau_1^* \propto \sqrt{\left(\frac{\xi}{\lambda}\right)^2 + \frac{8\xi}{\mathrm{Ca}}} + \frac{\xi}{\lambda}$. The second term τ_2^* is taken from the additional volume contributed by the filament generation prior to pinch-off. The additional volume is proportional to the product $\Delta a \times \Delta\omega$, where Δa can be assumed to be a constant (as shown in Fig. 8, a does not change much near pinch-off). Thus, we can estimate $\tau_2^* \propto \Delta\omega$. The third term, τ_3^*, is the additional necking time due to the leakage of CP through the corners. Thus, $\tau_3^* \propto \frac{\kappa}{q\mathrm{Ca}}\ln\left(\frac{q\tau^*}{l_0} + 1\right)$.

All the terms of Eq. (22) depend on Ca and are proportional to Ca^{-n}. Fitting of the generalized model $\tau^* = p + k\mathrm{Ca}^{-n}$ to the experimental data, with p, k, and n as the fitting parameters, yields n close to 0.5 (see the

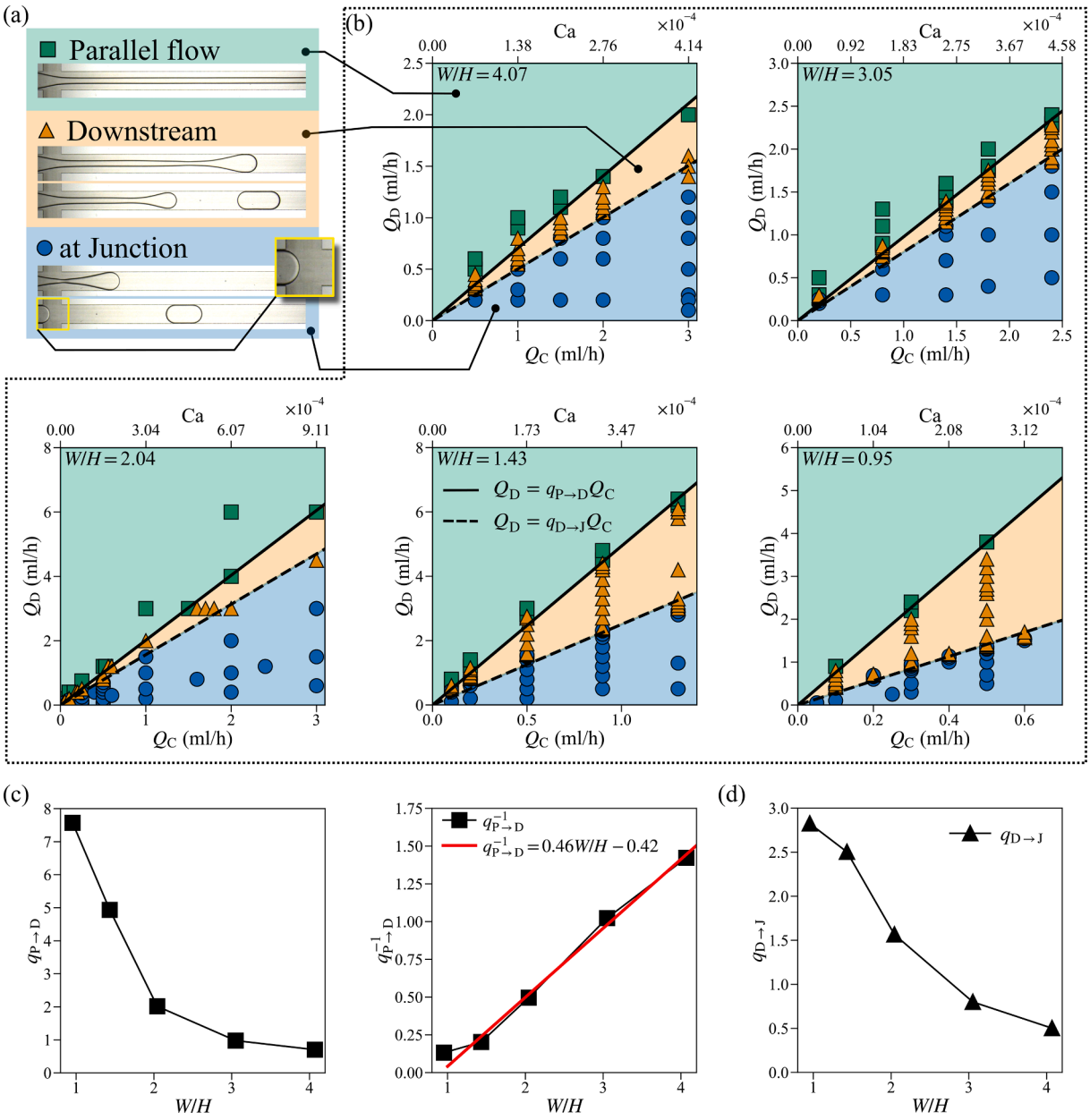

Fig. 10. Operating range for the three types of flow observed in the cross-junction devices with rectangular channels of different channel aspect ratios. (a) Experimental images showing the three observed flow types: formation of stable thread along the main channel – "Parallel Flow", formation of droplets downstream of the junction – "Downstream", and formation of droplets at the junction – "at Junction". For both droplet flow types, two images represent the forming droplet before (top) and after (bottom) pinch-off. For droplet formation at the junction, the interface fully recedes to the junction after pinch-off, as shown in the close-up image. (b) Maps illustrating the operating range for parallel flow (green squares), the formation of droplets downstream (yellow triangles) and at the junction (blue circles) for devices with different W/H. For each map, the transition between parallel flow and droplet formation downstream of the junction is shown by the solid black line ($Q_D = q_{P\to D} Q_C$). The transition between the two droplet formation types is shown by the dashed black line ($Q_D = q_{D\to J} Q_C$). (c) The influence of the channel aspect ratio on $q_{P\to D}$ (left) shows that the inverse of $q_{P\to D}$ is proportional to the aspect ratio (right). (d) Influence of the channel aspect ratio on the flow rate ratio $q_{D\to J}$ that demarcates the operating range for the flow type central to this work: droplet formation at the junction. Images were taken from experiment in the device $W/H = 4.07$. (For interpretation of the references to colour in this figure legend, the reader is referred to the web version of this article.)

inset in Fig. 2c and Fig. 3b). Additionally, the experimental data reveal a weak dependence on q. We have found that the fitted relation is the most related to τ_1^* in terms of both the exponent of the Ca dependence and negligible q dependence. This suggests that the mechanism of the elongation of the cosine shape of the neck is the dominant effect that constitutes the entire necking time τ^*. Thus, to include the dependency of τ^* on the flow rate condition, we assume a more straightforward form of τ^* as

$$\tau^* = \frac{\chi}{\sqrt{\mathrm{Ca}}} + p, \tag{23}$$

with χ and p as constant parameters that may be a function of channel geometry. Parameter p corresponds to τ^* of higher Ca values.

On the other hand, we also found that the leaking effect causes l_0 of Eq. (3) to be dependent on Ca, with $l_0(\mathrm{Ca}) \propto \mathrm{Ca}^{-1}$, as shown in Fig. 7b. To incorporate this dependency, we generalize the term l_0 as

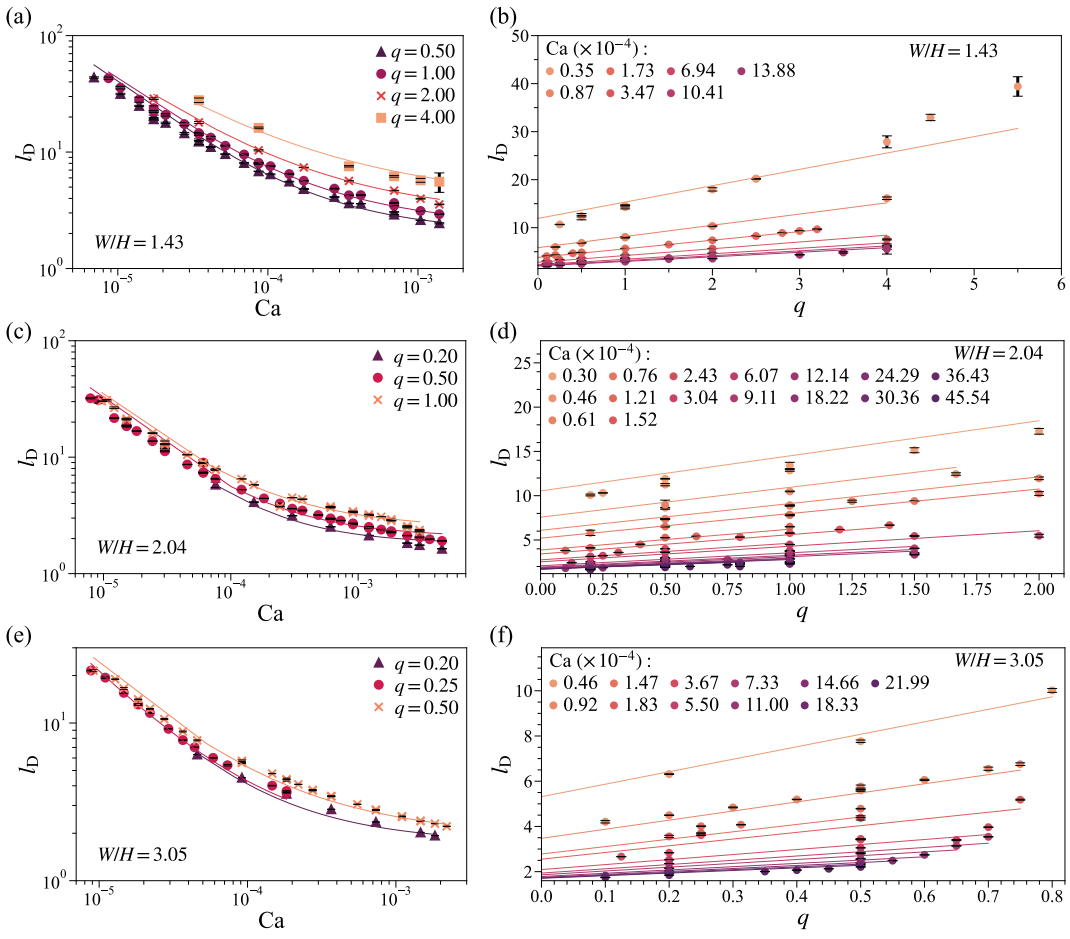

Fig. 11. Measurements (points) and theoretical predictions (solid lines) for devices with W/H: (a) and (b) 1.43; (c) and (d) 2.04; (e) and (f) 3.05. The fitting parameters based on each device W/H are (all coefficients are dimensionless): $W/H = 3.05$: $\chi = 3.46 \times 10^{-2}$, $p = 0.41$, $\lambda_0 = 1.63$, $\phi = 1.69 \times 10^{-4}$; $W/H = 2.04$: $\chi = 1.78 \times 10^{-2}$, $p = 0.74$, $\lambda_0 = 1.64$, $\phi = 2.70 \times 10^{-4}$; $W/H = 1.43$: $\chi = 1.72 \times 10^{-2}$, $p = 0.49$, $\lambda_0 = 1.68$,$\phi = 3.52 \times 10^{-4}$.

$$l_0 = \lambda_0 + \frac{\phi}{\mathrm{Ca}}, \tag{24}$$

where λ_0 and ϕ are constant parameters that may be a function of the microchannel geometry. By using Eqs. (23) and (24), we generalized Eq. (3) for the cross-junction device, as shown previously in Eq. (4).

4. Conclusions

We studied the formation of droplets in cross-junctions at low capillary numbers. We showed a lower limit of the squeezing regime, below which the strong Ca dependency in the volume of the generated droplets appears. In addition to the similarity in the leaking regime for droplet formation in cross- and T-junctions, this work reveals that there are also fundamental differences between these two types of junctions. These differences arise from the constraints on the interface of a forming droplet imposed by the geometry of the junction. In T-junctions, the shape of a forming droplet is constrained by the walls of the main and side channels, such that the critical shape at pinch-off solely depends on the total amount of the continuous phase collected behind the forming droplet and not on Ca. Without the constraint imposed by the walls of the side channel, the interface of a forming droplet in a cross-junction has more freedom to adjust its shape depending on the rate at which the continuous phase collects behind the forming droplet, such that the critical shape at pinch-off does depend on Ca. We generalized the classical squeezing law based on our findings, thereby quantifying and rationalizing the Ca dependencies in its parameters. This generalized model is in good agreement with the experimental data.

Considering practical implications, the described low Ca regime is the least favorable droplet generation method due to its extreme sensitivity to control parameters, notably flow rates, which significantly influence droplet volume. The presented work raises awareness of this issue and provides equations helping to identify the low boundary for the squeezing regime. Alternatively, as we have shown, a more robust (however, more complicated in fabrication) solution can be offered using a junction with circular channels, mitigating the risk of leaking and offering a broader spectrum of parameters for squeezing.

Declaration of Competing Interest

The authors declare that they have no known competing financial interests or personal relationships that could have appeared to influence the work reported in this paper.

Data availability

Data will be made available on request.

Acknowledgments

The project operated within the First Team grant (POIR.04.04.00-00-3FEF/17-00) of the Foundation for Polish Science, co-financed by the EU under the Smart Growth Operational Program. This publication is part of a project that has received funding from the European Union's Horizon 2020 research and the innovation programme under the Marie

Skłodowska-Curie grant agreement No. 711859. Scientific work was funded from the financial resources for science in the years 2017-2022, awarded by the Polish Ministry of Science and Higher Education for implementing an international co-financed project. P.G. acknowledges the support from the National Science Centre, Poland, where funding was based on decision 2018/30/A/ST4/00036, Maestro 10. We acknowledge support from National Science Centre Poland grants 2019/34/H/NZ6/00699 (Norwegian Financial Mechanism).

Appendix 1: Operating range for droplet formation

We identify the operating range in which droplets are formed in the five devices with channels of different aspect ratios W/H. We independently varied Q_C and Q_D and recorded the resulting flow regime.

We observed three types of flows, in line with earlier work [30]: formation of stable thread along the main channel – "Parallel Flow" (Fig. 10a, top or Supplementary Video 3), droplet formation downstream of the junction – "Downstream", (Fig. 10a, middle or Supplementary Video 2), and droplet formation at the junction – "at Junction" (Fig. 10a, bottom or Supplementary Video 1). The main difference between the two droplet formation regimes is in the position of the tip of the DP immediately after pinch-off. The tip of the DP either does not recede to the junction, as illustrated by the two images before and after pinch-off in Fig. 10a, middle, or does fully recede (see the two images in Fig. 10a, bottom).

Flow regime maps in terms of Q_C and Q_D are shown for channels with different aspect ratios in Fig. 10b. These maps show that parallel flow is generally observed for larger values, while droplet formation at the junction is observed for lower values of q. The two transitions between the three flow types can be approximated by two straight lines, i.e., for constant q. Let us introduce $q_{P\to D}$ as the value of q that corresponds to the transition between parallel flow and droplet formation downstream of the junction. Similarly, $q_{D\to J}$ corresponds to the transition between droplet formation downstream and at the junction. We obtained $q_{P\to D}$ and $q_{D\to J}$ from the maps in Fig. 10b for the channels with different aspect ratios. Parallel flow is observed for a broader range of operating conditions in shallower channels, as shown on the left side of Fig. 10c, in accordance with previous reports [45]. Following the arguments of Humphry et al. [23], we assume that the inverse of $q_{P\to D}$ can be approximated by a linear function of the aspect ratio for $W/H \gg 1$, i.e., $q_{P\to D}^{-1} = 0.46(W/H) - 0.45$ (with the coefficients obtained from a fit to the experimental data – see the right side of Fig. 10c). The transition between droplet formation downstream and at the junction also depends on W/H, with a more extensive operation range for droplet formation at the junction for less shallow channels (see Fig. 10d).

The main point of the analysis presented here is to illustrate that there is a W/H-dependent upper limit to the values of q for which the devices can be operated in the regime central to this paper: droplet formation at the junction.

Appendix 2: Additional experimental results

Fig. 11 shows the additional experimental results obtained from devices with aspect ratios that differ from those shown previously in Fig. 4. The points are the measurement results, whereas the solid lines are the curve-fitting results based on Eq. (4).

Appendix A. Supplementary data

Supplementary data to this article can be found online at https://doi.org/10.1016/j.cej.2023.145601.

References

[1] S.-Y. Teh, R. Lin, L.-H. Hung, A.P. Lee, Droplet microfluidics, Lab Chip 8 (2008) 198–220, https://doi.org/10.1039/B715524G.
[2] R. Seemann, M. Brinkmann, T. Pfohl, S. Herminghaus, Droplet based microfluidics, Rep. Prog. Phys. 75 (1) (2012), https://doi.org/10.1088/0034-4885/75/1/016601, 016601.
[3] L. Shang, Y. Cheng, Y. Zhao, Emerging Droplet Microfluidics, Chem. Rev. 117 (2017) 7964–8040, https://doi.org/10.1021/acs.chemrev.6b00848.
[4] G. Wu, Y. Zhao, X. Li, M.M. Ali, S. Jia, Y. Ren, L. Hu, Single-cell extracellular vesicle analysis by microfluidics and beyond, TrAC Trends Anal. Chem. 159 (2023), 116930, https://doi.org/10.1016/j.trac.2023.116930.
[5] W. Tang, M. He, B. Chen, G. Ruan, Y. Xia, P. Xu, G. Song, Y. Bi, B. Hu, Investigation of toxic effect of mercury on Microcystis aeruginosa: Correlation between intracellular mercury content at single cells level and algae physiological responses, Sci. Total Environ. 858 (2023), 159894, https://doi.org/10.1016/j.scitotenv.2022.159894.
[6] I. Bagemihl, C. Bhatraju, J.R. van Ommen, V. van Steijn, Electrochemical Reduction of CO2 in Tubular Flow Cells under Gas-Liquid Taylor Flow, ACS Sustain. Chem. Eng. 10 (2022) 12580–12587, https://doi.org/10.1021/acssuschemeng.2c03038.
[7] S. Jakiela, T.S. Kaminski, O. Cybulski, D.B. Weibel, P. Garstecki, Bacterial Growth and Adaptation in Microdroplet Chemostats, Angew. Chem. Int. Ed. 52 (2013) 8908–8911, https://doi.org/10.1002/anie.201301524.
[8] C.M. Ackerman, C. Myhrvold, S.G. Thakku, C.A. Freije, H.C. Metsky, D.K. Yang, S. H. Ye, C.K. Boehm, T.-S.-F. Kosoko-Thoroddsen, J. Kehe, T.G. Nguyen, A. Carter, A. Kulesa, J.R. Barnes, V.G. Dugan, D.T. Hung, P.C. Blainey, P.C. Sabeti, Massively multiplexed nucleic acid detection with Cas13, Nature 582 (2020) 277–282, https://doi.org/10.1038/s41586-020-2279-8.
[9] H. Takahara, H. Matsushita, E. Inui, M. Ochiai, M. Hashimoto, Convenient microfluidic cartridge for single-molecule droplet PCR using common laboratory equipment, Anal. Methods 13 (2021) 974–985, https://doi.org/10.1039/D0AY01779E.
[10] R. Salomon, D. Kaczorowski, F. Valdes-Mora, R.E. Nordon, A. Neild, N. Farbehi, N. Bartonicek, D. Gallego-Ortega, Droplet-based single cell RNAseq tools: a practical guide, Lab Chip 19 (2019) 1706–1727, https://doi.org/10.1039/C8LC01239C.
[11] G. Xing, J. Ai, N. Wang, Q. Pu, Recent progress of smartphone-assisted microfluidic sensors for point of care testing, TrAC Trends Anal. Chem. 157 (2022), 116792, https://doi.org/10.1016/j.trac.2022.116792.
[12] C.-X. Zhao, Multiphase flow microfluidics for the production of single or multiple emulsions for drug delivery, Adv. Drug Deliv. Rev. 65 (2013) 1420–1446, https://doi.org/10.1016/j.addr.2013.05.009.
[13] G.T. Vladisavljević, N. Khalid, M.A. Neves, T. Kuroiwa, M. Nakajima, K. Uemura, S. Ichikawa, I. Kobayashi, Industrial lab-on-a-chip: Design, applications and scale-up for drug discovery and delivery, Adv. Drug Deliv. Rev. 65 (2013) 1626–1663, https://doi.org/10.1016/j.addr.2013.07.017.
[14] K. Göke, T. Lorenz, A. Repanas, F. Schneider, D. Steiner, K. Baumann, H. Bunjes, A. Dietzel, J.H. Finke, B. Glasmacher, A. Kwade, Novel strategies for the formulation and processing of poorly water-soluble drugs, Eur. J. Pharm. Biopharm. 126 (2018) 40–56, https://doi.org/10.1016/j.ejpb.2017.05.008.
[15] H. Wang, Y. Liu, Z. Chen, L. Sun, Y. Zhao, Anisotropic structural color particles from colloidal phase separation, Sci. Adv. 6 (2020) eaay1438, https://doi.org/10.1126/sciadv.aay1438.
[16] X. Ye, Q. Fan, L. Shang, F. Ye, Adsorptive carbon-based materials for biomedical applications, Eng. Regen. 3 (2022) 352–364, https://doi.org/10.1016/j.engreg.2022.08.001.
[17] D. Carugo, E. Bottaro, J. Owen, E. Stride, C. Nastruzzi, Liposome production by microfluidics: potential and limiting factors, Sci. Rep. 6 (2016) 25876, https://doi.org/10.1038/srep25876.
[18] K. Muijlwijk, C. Berton-Carabin, K. Schroën, Cross-flow microfluidic emulsification from a food perspective, Trends Food Sci. Technol. 49 (2016) 51–63, https://doi.org/10.1016/j.tifs.2016.01.004.
[19] T. Cubaud, T.G. Mason, Capillary threads and viscous droplets in square microchannels, Phys. Fluids 20 (2008), 053302, https://doi.org/10.1063/1.2911716.

[20] W. Lee, L.M. Walker, S.L. Anna, Role of geometry and fluid properties in droplet and thread formation processes in planar flow focusing, Phys. Fluids 21 (2009), 032103, https://doi.org/10.1063/1.3081407.
[21] P. Garstecki, I. Gitlin, W. DiLuzio, G.M. Whitesides, E. Kumacheva, H.A. Stone, Formation of monodisperse bubbles in a microfluidic flow-focusing device, Appl. Phys. Lett. 85 (13) (2004) 2649–2651, https://doi.org/10.1063/1.1796526.
[22] P. Garstecki, H.A. Stone, G.M. Whitesides, Mechanism for Flow-Rate Controlled Breakup in Confined Geometries: A Route to Monodisperse Emulsions, Phys. Rev. Lett. 94 (2005), 164501, https://doi.org/10.1103/PhysRevLett.94.164501.
[23] K.J. Humphry, A. Ajdari, A. Fernández-Nieves, H.A. Stone, D.A. Weitz, Suppression of instabilities in multiphase flow by geometric confinement, Phys. Rev. E 79 (2009), 056310, https://doi.org/10.1103/PhysRevE.79.056310.
[24] Z. Cao, Z. Wu, B. Sundén, Dimensionless analysis on liquid-liquid flow patterns and scaling law on slug hydrodynamics in cross-junction microchannels, Chem. Eng. J. 344 (2018) 604–615, https://doi.org/10.1016/j.cej.2018.03.119.
[25] Z. Liu, M. Chai, X. Chen, S.H. Hejazi, Y. Li, Emulsification in a microfluidic flow-focusing device: Effect of the dispersed phase viscosity, Fuel 283 (2021), 119229, https://doi.org/10.1016/j.fuel.2020.119229.
[26] Z. Nie, M. Seo, S. Xu, P.C. Lewis, M. Mok, E. Kumacheva, G.M. Whitesides, P. Garstecki, H.A. Stone, Emulsification in a microfluidic flow-focusing device: effect of the viscosities of the liquids, Microfluid. Nanofluidics. 5 (2008) 585–594, https://doi.org/10.1007/s10404-008-0271-y.
[27] P. Garstecki, M.J. Fuerstman, H.A. Stone, G.M. Whitesides, Formation of droplets and bubbles in a microfluidic T-junction—scaling and mechanism of break-up, Lab Chip 6 (2006) 437–446, https://doi.org/10.1039/B510841A.
[28] X. Chen, T. Glawdel, N. Cui, C.L. Ren, Model of droplet generation in flow focusing generators operating in the squeezing regime, Microfluid. Nanofluidics. 18 (2015) 1341–1353, https://doi.org/10.1007/s10404-014-1533-5.
[29] S. van Loo, S. Stoukatch, M. Kraft, T. Gilet, Droplet formation by squeezing in a microfluidic cross-junction, Microfluid. Nanofluidics. 20 (2016) 146, https://doi.org/10.1007/s10404-016-1807-1.
[30] H. Liu, Y. Zhang, Droplet formation in microfluidic cross-junctions, Phys. Fluids 23 (2011), 082101, https://doi.org/10.1063/1.3615643.
[31] J. Tan, J.H. Xu, S.W. Li, G.S. Luo, Drop dispenser in a cross-junction microfluidic device: Scaling and mechanism of break-up, Chem. Eng. J. 136 (2008) 306–311, https://doi.org/10.1016/j.cej.2007.04.011.
[32] T. Fu, Y. Wu, Y. Ma, H.Z. Li, Droplet formation and breakup dynamics in microfluidic flow-focusing devices: From dripping to jetting, Chem. Eng. Sci. 84 (2012) 207–217, https://doi.org/10.1016/j.ces.2012.08.039.
[33] Q. Chen, J. Li, Y. Song, D.M. Christopher, X. Li, Modeling of Newtonian droplet formation in power-law non-Newtonian fluids in a flow-focusing device, Heat Mass Transf. 56 (2020) 2711–2723, https://doi.org/10.1007/s00231-020-02899-6.
[34] P.M. Korczyk, V. van Steijn, S. Blonski, D. Zaremba, D.A. Beattie, P. Garstecki, Accounting for corner flow unifies the understanding of droplet formation in microfluidic channels, Nat. Commun. 10 (2019) 2528, https://doi.org/10.1038/s41467-019-10505-5.
[35] H. Wong, C.J. Radke, S. Morris, The motion of long bubbles in polygonal capillaries. Part 1. Thin films, J. Fluid Mech. 292 (1995) 71–94, https://doi.org/10.1017/S0022112095001443.
[36] P.M. Korczyk, O. Cybulski, S. Makulska, P. Garstecki, Effects of unsteadiness of the rates of flow on the dynamics of formation of droplets in microfluidic systems, Lab Chip 11 (2010) 173–175, https://doi.org/10.1039/C0LC00088D.
[37] K.G. Biswas, R. Patra, G. Das, S. Ray, J.K. Basu, Effect of flow orientation on liquid–liquid slug flow in a capillary tube, Chem. Eng. J. 262 (2015) 436–446, https://doi.org/10.1016/j.cej.2014.09.122.
[38] S. van der Walt, J.L. Schönberger, J. Nunez-Iglesias, F. Boulogne, J.D. Warner, N. Yager, E. Gouillart, T. Yu, the scikit-image contributors, scikit-image: image processing in Python, PeerJ 2 (2014) e453, https://doi.org/10.7717/peerj.453.
[39] C.R. Harris, K.J. Millman, S.J. van der Walt, R. Gommers, P. Virtanen, D. Cournapeau, E. Wieser, J. Taylor, S. Berg, N.J. Smith, R. Kern, M. Picus, S. Hoyer, M.H. van Kerkwijk, M. Brett, A. Haldane, J.F. del Río, M. Wiebe, P. Peterson, P. Gérard-Marchant, K. Sheppard, T. Reddy, W. Weckesser, H. Abbasi, C. Gohlke, T.E. Oliphant, Array programming with NumPy, Nature 585 (2020) 357–362, https://doi.org/10.1038/s41586-020-2649-2.
[40] P. Virtanen, R. Gommers, T.E. Oliphant, M. Haberland, T. Reddy, D. Cournapeau, E. Burovski, P. Peterson, W. Weckesser, J. Bright, S.J. van der Walt, M. Brett, J. Wilson, K.J. Millman, N. Mayorov, A.R.J. Nelson, E. Jones, R. Kern, E. Larson, C. J. Carey, İ. Polat, Y. Feng, E.W. Moore, J. VanderPlas, D. Laxalde, J. Perktold, R. Cimrman, I. Henriksen, E.A. Quintero, C.R. Harris, A.M. Archibald, A.H. Ribeiro, F. Pedregosa, P. van Mulbregt, SciPy 1.0: fundamental algorithms for scientific computing in Python, Nat. Methods 17 (2020) 261–272, https://doi.org/10.1038/s41592-019-0686-2.
[41] M. Newville, T. Stensitzki, D.B. Allen, A. Ingargiola, LMFIT: Non-Linear Least-Square Minimization and Curve-Fitting for Python, 2014, https://doi.org/10.5281/zenodo.11813.
[42] J.D. Hunter, Matplotlib: A 2D Graphics Environment, Comput. Sci. Eng. 9 (2007) 90–95, https://doi.org/10.1109/MCSE.2007.55.
[43] E. van der Velden, CMasher: Scientific colormaps for making accessible, informative and “cmashing” plots, J. Open Source Softw. 5 (2020) (2004), https://doi.org/10.21105/joss.02004.
[44] N.A. Mortensen, F. Okkels, H. Bruus, Reexamination of Hagen-Poiseuille flow: Shape dependence of the hydraulic resistance in microchannels, Phys. Rev. E 71 (2005), 057301, https://doi.org/10.1103/PhysRevE.71.057301.
[45] Y. Son, N.S. Martys, J.G. Hagedorn, K.B. Migler, Suppression of Capillary Instability of a Polymeric Thread via Parallel Plate Confinement, Macromolecules 36 (2003) 5825–5833, https://doi.org/10.1021/ma0343986.